Particle laden flows around a circular cylinder from the hydrodynamic to granular regime

D. Schuster, Eric Climent, U. Rüde

To cite this version:

D. Schuster, Eric Climent, U. Rüde. Particle laden flows around a circular cylinder from the hydrodynamic to granular regime. International Journal of Multiphase Flow, 2023, 165, pp.104487. 10.1016/j.ijmultiphaseflow.2023.104487 . hal-04593434

HAL Id: hal-04593434

https://ut3-toulouseinp.hal.science/hal-04593434v1

Submitted on 29 May 2024

Particle laden flows around a circular cylinder from the hydrodynamic to granular regime

D. Schuster[a,b], E. Climent[a], U. Rüde[b,c]

[a] *Institut de Mécanique des Fluides de Toulouse, IMFT, Université de Toulouse, CNRS, France*
[b] *CERFACS, 42 avenue Gaspard Coriolis, 31057 Toulouse, France*
[c] *Chair for Computer Science 10 - System simulation, Friedrich-Alexander-Universität Erlangen-Nürnberg, Cauerstraße 11, 91058 Erlangen, Germany*

Abstract

The flow around a circular cylinder is studied with the presence of solid finite-size spherical particles. The simulations of suspension flows are based on highly efficient simulation algorithms to generate scalable Lattice Boltzmann Method calculations. Simulations of particle resolved dynamics with up to 4,800 million grid cells and 1.8 million spherical particles are carried out for different flow regimes and particle concentrations (from dilute, 5% volume concentration to semi-dilute regime, 20%). We investigated a range of parameters that spans from suspensions of iso-dense particles to highly inertial particles in a granular flow, while considering particle to cylinder diameter ratios of 5 and 10.

The flow response is described by characteristic properties such as vortex shedding frequency or wake recirculation length. Flow regimes with iso-dense particles can be rationalized by means of mixture material properties while we observe a progressive transition to granular flow for inertial particles. Drag and lift forces acting onto the cylinder are presented in time and frequency domains and the physical analysis is based on the respective hydrodynamic and particle collision contributions.

Keywords: Lattice-Boltzmann method, Dispersed Two Phase Flow, High Performance Computing, Rigid Body Dynamics

---

1. Introduction

Dispersed two-phase flows are a widespread fluid dynamics situation that is encountered in various industrial (petroleum or nuclear engineering, concrete, food products, cosmetics and pharmacy) and natural processes (river flow, avalanches, dust storms) and even in biological fluids like blood. Suspensions of non-Brownian particles and granular flows are known to exhibit intricate behavior in response to shear flows. A large portion of today's energy transformation still relies on burning fossil fuels. Pulverized coal combustion is a gas-solid flow, that has been intensively studied to improve numerical predictions [1]. These simulation methods can be used to enhance efficiency of burners and boilers, such as the circulating fluidized bed [2, 3]. There have been recent efforts to compute small scale models with a few thousands particles by means of direct numerical simulation (DNS) [4, 5]. Particulate flows are also found in environmental engineering, such as sediment transport and dune formation in riverbeds [6] or erosion processes in geomorphological patterns [7].

Dragging a plow in soil [8, 9], and mixing particles with an impeller [10, 11] are situations involving a moving obstacle in a granular medium. Predicting the forces experienced by the object and the flow around it is an important issue. This has been commonly investigated for single phase fluids, but these issues remain mostly open in the case of a granular medium or particulate flowing suspensions. For industrial applications, such as filtration and coagulation of aerosols, slurry transport, the interstitial viscous fluid may have a major effect on the flow structure and the results interactions with the obstacle. The shape of a circular cylinder is obviously very generic for such situations. For fibrous filtration systems (fibers are typically cylindrically shaped). The presence of cylinders occurs also in two-phase flow reactors in oil refineries, during dip coating processes [12, 13], and in so-called fog harvesting when liquid films are formed on the collecting wires [14]. Sediment transport around anchoring apparatus [15] is another example of particulate flows around cylindrical shape obstacles [16]. The rheological characteristics of flowing materials have a strong influence on the drag force, which can thus be very different from single phase fluids. The geometric configuration of a cylindrical object embedded in a granular flow or particulate suspensions is of fundamental interest to probe the rheology [17] of those two-phase systems. In medical research, red blood cells can be modeled by extending the numerical model to allow interfaces to deform. A combination of the Lattice Boltzmann Method (LBM), immersed boundary method and finite element method has been used to simulate blood flow through an array of cylindrical obstacles [18].

The insights gained by particle resolved simulations can help to improve closure models such as the discrete particle method (DPM), where the size of particles is typically much smaller than the computational grid, and the two fluids model (TFM), where both fluid and solid phases are represented as a continuum. In large scale industrial applications this Eulerian-Eulerian approach is usually the only viable option due to the high computational demands of particle resolved methods. We are aiming at providing information on the flow response due to the presence of particles by means of numerical simulations. The flow around a cylinder is one of the most generic flow configurations and it is well documented for the single phase configuration. By adding solid particles into the fluid we want to understand the interplay between fluid transport, particle inertia and collisions among individual particles as well as with the obstacle.This information is particularly relevant because the flow contains regions of particle impact in front of the obstacle and shear layers in the wake.

Granular flows around obstacles have been studied experimentally [19], [20] and numerically [21]. The granular phase in our simulations is resolved with a discrete element method (DEM) and tested against granular flow experiments [22] and numerical simulations [23, 24]. The physics changes when considering liquids instead of air as the carrying fluid (density ratio becomes close to unity for most solid materials), as shown by experiments of grain-water flows around a cylinder [25]. The presence of liquid (wet granular flow) modifies significantly the flow behavior compared to granular media in the same situation [22]. Indeed, for dry granular flows the interaction between the cylinder and the surrounding particles is mediated by normal impact and multibody friction contacts. Two-dimensional simulations of a sphere towed at constant velocity into smaller spherical grains without gravity have shown the presence of a dense granular cluster in front of the moving object [26]. The drag force exerted by the grains on the moving obstacle increases linearly with particle concentration and no divergence is observed while approaching dense packing. In addition to the drag, added-mass force have been evidence in 2D simulations of dry granular matter experiencing surrounding flow oscillations ([27]) If the density ratio between particles and fluid is high and the suspension is sufficiently dilute, there are only few interactions among particles and the fluid flow is unaffected by the presence of particles. Under these assumptions it is relevant to use one-way coupling model of interaction between fluid and solid phases [28, 29, 30].

In this study, we make use of a fully-coupled approach, where fluid-particle and particle-particle interactions plus the feedback effect of particles on the fluid flow are simulated. Numerical simulations using Lattice Boltzmann Method (LBM) have been conducted for suspension over an obstacle at Reynolds numbers well below the onset of unsteadiness [31]. They observed that isolated finite size particles released inside the recirculating wake region migrate towards a stable limit cycle at the boundary between wake and free stream. At low concentration, the wake remains depleted of particles. At higher particle density the limit cycle becomes unstable due to the particle's increased inertia [32]. Eventually this process will deplete the wake of particles, especially for particles of larger size. With many particles the hydrodynamic interactions and collisions among flowing particles can cause trajectory fluctuations which lead to an exchange of particles between the wake and the free stream.

Gravity is neglected to focus on the effect of particle inertia on the flow structure. The relation between fluid flow velocity and terminal settling velocity due to gravity strongly depends on the particle size and density ratio. For iso-dense particles, gravity obviously has no role. Let's consider the example of a solid-liquid suspension composed of water for the carrying fluid and a typical flow Reynolds number of 100. For particles smaller than 50 microns in diameter even iron particles have settling velocity corresponding to less than 2% of the fluid velocity. For glass and iron particles with 100 microns diameter, the ratio goes up to 15%. The only case, for which gravity may have a drastic effect, is when density ratio raises up to 100 (or even higher, for liquid-gas or solid-gas flows).

Our work will utilize the two-phase particle resolved LBM coupled with a discrete element method to investigate this generic configuration over a wide range of Reynolds numbers and particle inertia to highlight the specific response of the fluid-solid mixture around an obstacle. We will test the applicability and limits of the assumption that a suspension can be interpreted as an equivalent Newtonian fluid whose viscosity and density depend on particle loading in the range of dilute to semi-dilute regime.

The paper is organized as follows. One section is dedicated to the presentation of the numerical methods together with validations for single and two-phase flows. This section contains the details on our numerical setup. Then, simulation results are analyzed by varying the Reynolds number of the flow yielding both steady and unsteady flows. The effect of the particulate volume concentration is investigated over dilute and moderately concentrated regimes up to 20% volume concentration. Simulations are compared to experiments from literature and a discussion section details the transition from hydrodynamic to granular flow response and specific contributions to the drag. The paper is closed by the conclusion section.

2. Numerical methods and validation

2.1. Lattice-Boltzmann method

The Lattice Boltzmann Method (LBM) is a mesoscopic approach that can recover the macroscopic physics of the Navier-Stokes equations under certain conditions. Discretizing the lattice Boltzmann equation gives a statistical description of fictive particles colliding and propagating on a Cartesian lattice along a discrete set of velocities. The distribution function $f_\alpha(\boldsymbol{c}_\alpha, \boldsymbol{x}, t)$ corresponds to the probability density of particles moving at velocity $\boldsymbol{c}_\alpha$ in lattice direction α of a cell with cell center position $\boldsymbol{x}$ at time t. For all following simulations, the so-called *D3Q19* stencil [33] with 19 discrete velocities $\boldsymbol{c}_\alpha, \alpha \in 0...18$ is used. The algorithm for solving the lattice Boltzmann equation can be divided into a collision step

$$\tilde{f}_\alpha(\boldsymbol{x}, t) = f_\alpha(\boldsymbol{x}, t) + \Omega_\alpha(\boldsymbol{x}, t), \tag{1}$$

with the collision operator ω_α and the relaxation frequency τ, and a subsequent streaming step

$$f_\alpha(\boldsymbol{x} + \boldsymbol{c}_\alpha \Delta t, t + \Delta t) = \tilde{f}_\alpha(\boldsymbol{x}, t) \tag{2}$$

that propagates the updated set of distribution functions to neighboring cells $\boldsymbol{x} + \boldsymbol{c}_\alpha \Delta t$ and advances the simulation by time step Δt. During the collision the distribution functions are relaxed towards the local equilibrium

$$f_\alpha^{\mathrm{eq}}(\boldsymbol{u}, \rho) = w_\alpha \rho \left(1 + \frac{\boldsymbol{c}_\alpha \cdot \boldsymbol{u}}{c_s^2}) + \frac{(\boldsymbol{c}_\alpha \cdot \boldsymbol{u})^2}{2c_s^4} - \frac{\boldsymbol{u} \cdot \boldsymbol{u}}{2c_s^2} \right), \tag{3}$$

where w_α are the stencil specific lattice weights (see [33]) and c_s is the lattice speed of sound. More specifically, we use a formulation of the equilibrium distribution, which is suitable for small deviation from the reference pressure $\rho_0 = \rho - \rho'$ and better approximates the incompressible flow equations [34]:

$$f_\alpha^{\mathrm{eq}}(\boldsymbol{u}, \rho) = \omega_\alpha \left(\rho + \rho_0 \left[\frac{\boldsymbol{c}_\alpha \cdot \boldsymbol{u}}{c_s^2}) + \frac{(\boldsymbol{c}_\alpha \cdot \boldsymbol{u})^2}{2c_s^4} - \frac{\boldsymbol{u} \cdot \boldsymbol{u}}{2c_s^2} \right] \right). \tag{4}$$

Macroscopic values are recovered as moments of the distribution functions

$$\rho = \sum_\alpha f_\alpha, \quad \boldsymbol{u} = \frac{1}{\rho} \sum_\alpha \boldsymbol{c}_\alpha f_\alpha, \tag{5}$$

and the relaxation frequency is connected to the fluid kinematic viscosity

$$\nu = c_s^2 \left(\tau - \frac{1}{2} \right) \tag{6}$$

in the Navier-Stokes equations. For our simulations of particle-laden flow around a cylinder, we employ the classic single relaxation time (SRT) collision operator

$$\Omega_\alpha^{\mathrm{BGK}} = -\frac{1}{\tau} \left(f_\alpha - f_\alpha^{\mathrm{eq}} \right) \tag{7}$$

proposed by Bhatnagar, Gross and Krook (BGK) [35].

Preliminary tests have been conducted with the two relaxation times (TRT) model [36]. Distribution functions are split into symmetric and antisymmetric parts

$$f_\alpha^\pm = \frac{1}{2} \left(f_\alpha \pm f_{\bar{\alpha}} \right), \quad f_\alpha^{\mathrm{eq}\pm} = \frac{1}{2} \left(f_\alpha^{\mathrm{eq}} \pm f_{\bar{\alpha}}^{\mathrm{eq}} \right) \tag{8}$$

with $\bar{\alpha}$ denoting the inverse direction, i.e. $c_{\bar{\alpha}} = -c_\alpha$. The TRT collision operator can be written as

$$\Omega_\alpha^{\mathrm{TRT}} = -\frac{1}{\tau^+} \left(f_\alpha^+ - f_\alpha^{\mathrm{eq}+} \right) - \frac{1}{\tau^-} \left(f_\alpha^- - f_\alpha^{\mathrm{eq}-} \right) \tag{9}$$

and involves the two distinct relaxation times τ^+, τ^-. While τ^+ is responsible for the kinematic fluid viscosity $\nu = c_s^2 \left(\tau^+ - \frac{1}{2} \right)$, the second relaxation time τ^- can be chosen in a way that improves accuracy and stability. The relation between these two is the so-called "magic parameter"

$$\Lambda = \left(\frac{1}{2} - \tau^+ \right) \left(\frac{1}{2} - \tau^- \right). \tag{10}$$

Setting $\Lambda = 3/16$ has been shown to produce the correct velocity profile for the Poiseuille flow when using bounce-back boundary schemes [37], whereas the best stability in a generic simulation can be achieved via $\Lambda = 1/4$ [38]. For a comprehensive description of derivation and implementation of the LBM we refer to Krüger et al. [39].

Forces due to particle laden flows on the cylinder (which will be discussed in the following sections) have been simulated with both SRT an TRT model for the three particle materials (i.e. hydrogel, glass and iron) and two distinct Reynolds numbers (i.e. 50 and 150). We can observe weak variations of the different contributions to the drag and lift forces acting on the cylinder. TRT induces slightly higher drag from particle collisions, but lower drag from fluid resulting in a relative difference of the total suspension flow lower than 2%. The largest difference is lower than 5% for the case with iron particles and Reynolds equal to 150. Differences in the RMS of the lift coefficient are slightly higher from 3 to 6%). The values of the Strouhal numbers for the comparison between SRT and TRT stand within 1% difference except for the case with iron particles at Reynolds equal to 50 where it is 4%.

2.2. Momentum exchange method

Due to the kinetic nature of the LBM, momentum exchange between fluid and solid phases can be computed in a straightforward manner. The underlying idea is that mass components streaming into the boundary causes a momentum influx, while mass components streaming out of the boundary causes a momentum outflux. At the same time a no-slip condition has to be satisfied at the solid surface. The interface coupling is based on [40] and has been improved by [41]. In our configuration, solid particles, as well as the steady cylinder, are explicitly mapped into the domain as solid moving or fixed obstacles. The boundary treatment is executed for every discrete direction or link between fluid and solid nodes. The boundary condition along the fluid-solid interface is derived from a bounce back scheme

$$f_{\bar{\alpha}}(\boldsymbol{x}, t + \Delta t) = \tilde{f}_{\alpha}(\boldsymbol{x}, t) - 2\frac{w_\alpha}{c_s^2}\rho \boldsymbol{u}(\boldsymbol{x}_b, t) \cdot \boldsymbol{c}_\alpha, \tag{11}$$

which is extended by a term that takes the velocity $\boldsymbol{u}(\boldsymbol{x}_b, t)$ on the exact boundary location $\boldsymbol{x}_b = \boldsymbol{x} + \boldsymbol{c}_\alpha \delta_\alpha$ into account ($\boldsymbol{u}(\boldsymbol{x}_b, t)$ is zero for a fixed obstacle but equal to the solid body velocity for a moving particle). The variable δ_α is the relative distance between the cell center and the exact surface position. To achieve second order accuracy, we use the central linear interpolation (CLI) [36] given by

$$f_{\bar{\alpha}}(\boldsymbol{x}) = \tilde{f}_{\alpha}(\boldsymbol{x}) + \kappa_0 \left(\tilde{f}_{\alpha}(\boldsymbol{x} - \boldsymbol{c}_\alpha) - \tilde{f}_{\bar{\alpha}}(\boldsymbol{x}) \right) - \alpha \tfrac{w_\alpha}{c_s^2} \rho \boldsymbol{u}(\boldsymbol{x}_b) \cdot \boldsymbol{c}_\alpha, \tag{12}$$

with the coefficients $\kappa_0 = (1 - 2\delta_\alpha)/(1 + 2\delta_\alpha)$ and $\alpha = (1 + 2\delta_\alpha)$. This interpolation scheme uses subgrid information to smoothen the staircase approximation of the particle shape. It also involves the population at the node $\boldsymbol{x} - \boldsymbol{c}_\alpha$ which is located one cell further away from the particle boundary. The interaction force is the difference between instreaming and outstreaming mass components multiplied with the relative velocity between fluid and solid phases. It is calculated as

$$\boldsymbol{F}^{\alpha_{\mathrm{f-s}}}(\boldsymbol{x}_b, t) = \tfrac{(\Delta x)^3}{\Delta t} \left[(\boldsymbol{c}_{\alpha_{\mathrm{f-s}}} - \boldsymbol{u}(\boldsymbol{x}_b, t)) \tilde{f}_{\alpha_{\mathrm{f-s}}}(\boldsymbol{x}, t) - (\boldsymbol{c}_{\bar{\alpha}_{\mathrm{f-s}}} - \boldsymbol{u}(\boldsymbol{x}_b, t)) f_{\bar{\alpha}_{\mathrm{f-s}}}(\boldsymbol{x}, t + \Delta t) \right] \tag{13}$$

for every direction $\alpha_{\mathrm{f-s}}$ that links a fluid with a solid cell [40, 42]. Summing up the contributions over all fluid-solid links gives us the total force

$$\boldsymbol{F}_{\mathrm{f-s}}(t) = \sum_{\boldsymbol{x}_b} \sum_{\alpha_{\mathrm{f-s}}} \boldsymbol{F}^{\alpha_{\mathrm{f-s}}}(\boldsymbol{x}_b, t) \tag{14}$$

and torque

$$\boldsymbol{T}_{\mathrm{f-s}}(t) = \sum_{\boldsymbol{x}_b} \sum_{\alpha_{\mathrm{f-s}}} (\boldsymbol{x}_b - \boldsymbol{X}_p) \times \boldsymbol{F}^{\alpha_{\mathrm{f-s}}}(\boldsymbol{x}_b, t) \tag{15}$$

acting on a spherical particle with its center at position $\boldsymbol{X}_p$. Therefore, both translational and rotational motions of the particles are simulated. Due to the motion of a particle through the static computational grid, the domain mapping has to be adjusted. When a cell that was filled with fluid in the previous time step is now occupied by a particle, the cell status is simply changed to solid. In the case of a cell turning into a fluid cell, the missing distribution functions need to be reconstructed. They are set to the equilibrium distribution $f_\alpha^{\mathrm{eq}}(\rho, \boldsymbol{u})$, using the particle velocity $\boldsymbol{u}_p$ and an average density ρ of surrounding fluid cells. Additional information on this implementation can be found in Götz [43] or Bartuschat [44]. There are alternative approaches available, i.e. different formulations of the boundary condition and sophisticated algorithms for reconstructing missing distribution function of empty cells [45, 46].

To validate our method we investigate the particle's unsteady response to an external oscillatory force $\boldsymbol{F}_{\mathrm{ext}} = 3\pi\mu d\boldsymbol{u}_0 \sin(\omega t)$, where $\omega/2\pi$ is the oscillation frequency, $\boldsymbol{u}_0$ is a constant vector and μ is the dynamic fluid viscosity. A single finite-size sphere is embedded in a viscous fluid at rest with no gravity present. The theoretical particle velocity can be obtained by solving the Maxey-Riley equation [47]

$$\begin{aligned} m_p \frac{d\boldsymbol{u}_p}{dt} =& - 3\pi d \rho_f \nu \left(\boldsymbol{u}_p - \boldsymbol{u}_f\right) + m_f \frac{D\boldsymbol{u}_f}{Dt} + \frac{m_f}{2}\left(\frac{D\boldsymbol{u}_f}{Dt} - \frac{d\boldsymbol{u}_p}{dt}\right) \\ & - \frac{3}{2} d^2 \rho_f \sqrt{\pi\nu} \int_{t_0}^{t} \frac{1}{\sqrt{t-\tau}} \left(\frac{d\boldsymbol{u}_p}{d\tau} - \frac{d\boldsymbol{u}_f}{d\tau}\right) d\tau, \end{aligned} \tag{16}$$

following the approach of Wang et al. [48]. Eq. (16) is only valid for the Stokes regime (Re $\ll$ 1) and does not incorporate the Faxén terms in added mass, drag and history force contributions. For particle laden flow around a cylinder, although the Reynolds number considering particle diameter and slip velocity with the flow is small (below 10), the Reynolds number considering the cylinder diameter and inflow velocity is moderate (from 10 to 200).

The resulting oscillating motion of the particle is expressed as

$$\boldsymbol{u}_p(t) = \alpha \boldsymbol{u}_0 \sin(\omega t + \varphi), \tag{17}$$

with amplitude α and phase shift φ. When the particle is embedded in a quiescent fluid, the analytic solution gives a relation between the amplitude of external oscillatory forcing (written as $F(t) = \widehat{F} e^{i\omega t}$) and the particle velocity as

$$\widehat{F} = \widehat{u}_p \left[(m_p + \frac{1}{2} m_f) i\omega + 3\pi\mu d(1 + \delta e^{i\pi/4}) \right] e^{i\varphi}. \tag{18}$$

The terms on the right hand side of eq. (18) correspond respectively to particle inertia, added mass, steady drag and unsteady history forces. The contribution of Basset history force is important when the particle-to-fluid density ratio is low to moderate (typically below 10). The amplitude and phase shift of the particle velocity are presented in Fig. 1 for particle-fluid density ratios ρ_p/ρ_f up to 5 with $\psi^2 = \omega d^2/\nu$. The purely viscous contribution of the hydrodynamic force (in the absence of added mass term) is also plotted. The dimensionless frequency ψ^2 can be interpreted as a Stokes number corresponding to the ratio of the particle relaxation time to the fluid oscillation time scale. It is also the square of the ratio of the particle diameter to the Stokes layer thickness due to unsteady diffusion of momentum. The cubic simulation domain spans 10 particle diameters and is periodic in all directions.

Our fluid-solid-coupling approach delivers good results for a resolution of $d/\Delta\mathrm{x} = 20$, but exhibits a slight overestimation of amplitude and significant underestimation of the phase shift for $d/\Delta\mathrm{x} = 10$. Indeed, for high ψ^2, the Stokes layer is too thin to be accurately resolved. The deviation is stronger for smaller particle density and faster oscillation. It is clear that LBM predictions become gradually closer to the theoretical prediction while particle density is increased because the relative contribution of unsteady Basset drag reduces.

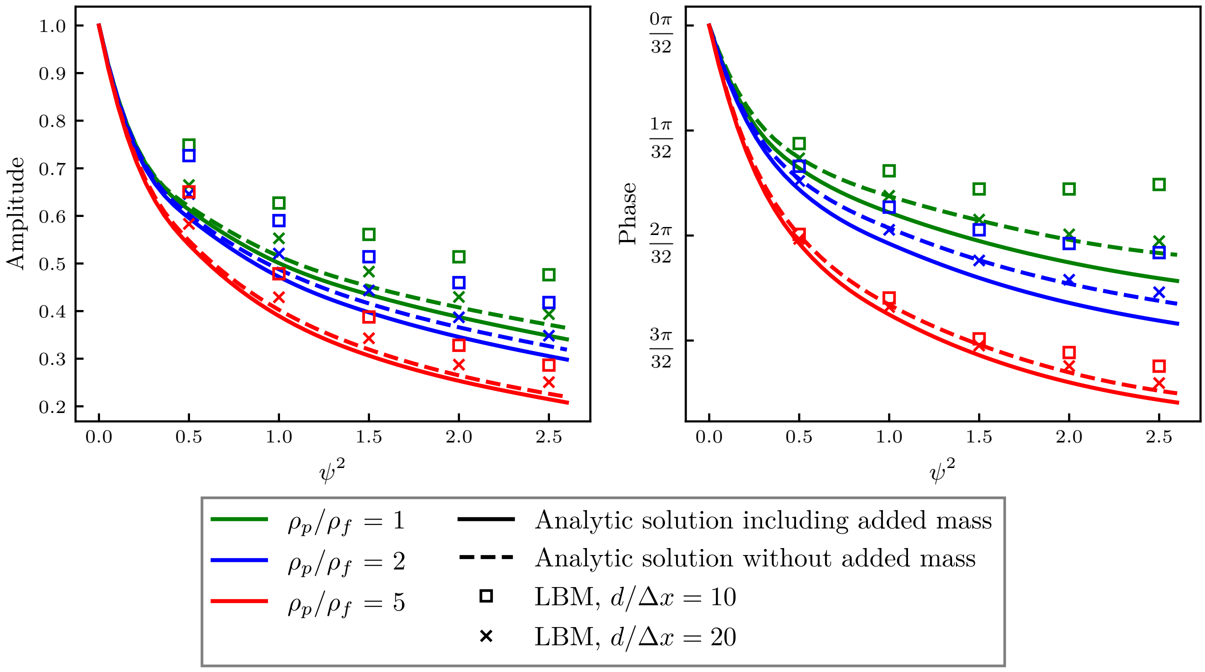

Figure 1: Amplitude and phase shift of external force to particle velocity. $\psi^2 = \omega d^2/\nu$ is the dimensionless frequency. The resolution is given by the number of lattice cells per particle diameter $d/\Delta\mathrm{x}$.

2.3. Granular collision modeling

Whenever an overlap between two particles is detected, a collision response needs to be modeled. A well established method for resolving collisions is the Discrete Element Method (DEM) [49, 50]. There are many variants of the DEM with complex physics modeling. Here, the so-called soft-sphere approach is used to compute the repulsive force for two spheres or a sphere and the cylinder. The penetration distance ϵ should be kept small in comparison to the particle diameter to ensure numerical stability and physical relevance [51]. The normal contact force

$$F_c^n = \max(0, k_n\epsilon - \gamma_n u_n) \tag{19}$$

is modeled based on a linear spring-dashpot system with normal spring stiffness k_n, normal damping coefficient γ_n and relative velocity in normal direction $u_n = \frac{\boldsymbol{n}}{\|\boldsymbol{n}\|} \cdot (\boldsymbol{u}_i - \boldsymbol{u}_j)$. Here, $\boldsymbol{u}_i$ and $\boldsymbol{u}_j$ correspond to

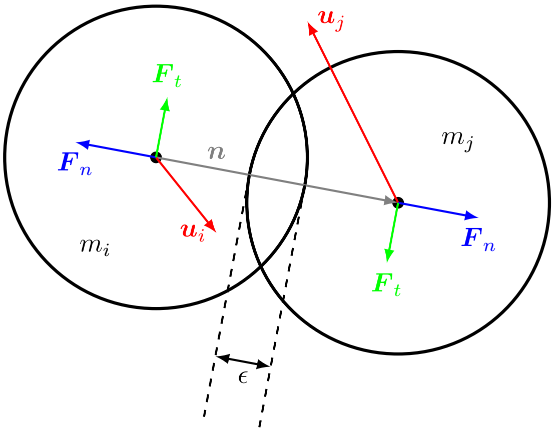

Figure 2: Scheme showing two colliding spherical particles

the velocity of particle i and particle j, respectively. F_c^n is restricted to positive values to avoid attractive forces and added to all interacting objects through positive summation. The computation of friction laws is specific for static and dynamic friction. Coulomb's friction law $F_c^t = \mu F_c^n$ is only applicable for two particles in contact, moving with a substantial relative tangential velocity. In the model of Haff and Werner [52] the force component F_c^t at low tangential velocity is interpreted as a shear damping model

$$F_c^t = -\min(\mu F_c^n, \gamma_t u_t) \tag{20}$$

with μ denoting the Coulomb friction parameter, γ_t denoting the tangential damping coefficient and $u_t = \| \left(\boldsymbol{u}_i - \boldsymbol{u}_j\right) - u_n \frac{\boldsymbol{n}}{\|\boldsymbol{n}\|} \|$ denoting the relative velocity in tangential direction. The Coulomb friction sets the upper limit for friction forces in this approach. Contact parameters, such as spring stiffness k_n and damping coefficient

$$\gamma_n = -2\sqrt{m_{ij} k_n} \frac{\ln e}{\sqrt{\pi^2 + \ln^2 e}} \tag{21}$$

are related to the coefficient of restitution e and the effective mass $m_{ij} = \frac{m_i m_j}{m_i + m_j}$ between particle i and particle j [53]. The time span of a typical collision

$$T_c = \frac{2\pi m_{ij}}{\sqrt{4 m_{ij} k_n - \gamma_n^2}} \tag{22}$$

can be estimated following [54].

The particle motion is integrated in time with a first-order semi-implicit Euler method. The particle velocity $\dot{v}_p = \frac{F}{m_p}$ is updated by using the total force F, which is obtained from fluid-solid interaction and collision. The angular acceleration $\dot{w}_p = \frac{T}{I}$ depends on the total torque T and the moment of inertia of a sphere $I = md^2/10$.

The coefficient of restitution is a material property related to the elasticity of a collision between two objects. The values for the materials used in this study are found in Tab. 1. Normal and tangential damping coefficients are assumed equal $\gamma_t = \gamma_n$. When interacting with a fixed obstacle, corresponding to the cylinder, the effective mass m_{ij} is equal to the particle mass only. Choosing a value for T_c will determine stiffness and damping coefficients via Eq. (21). In order to accurately resolve a solid collision, the granular time step Δt_G is commonly set about an order of magnitude smaller than the time step of the fluid solver Δt. We use a sub-stepping strategy to reduce the computational cost, while hydrodynamic force and torque are kept constant for a number $N_{sub} = \Delta t / \Delta t_G$ of sub-intervals.

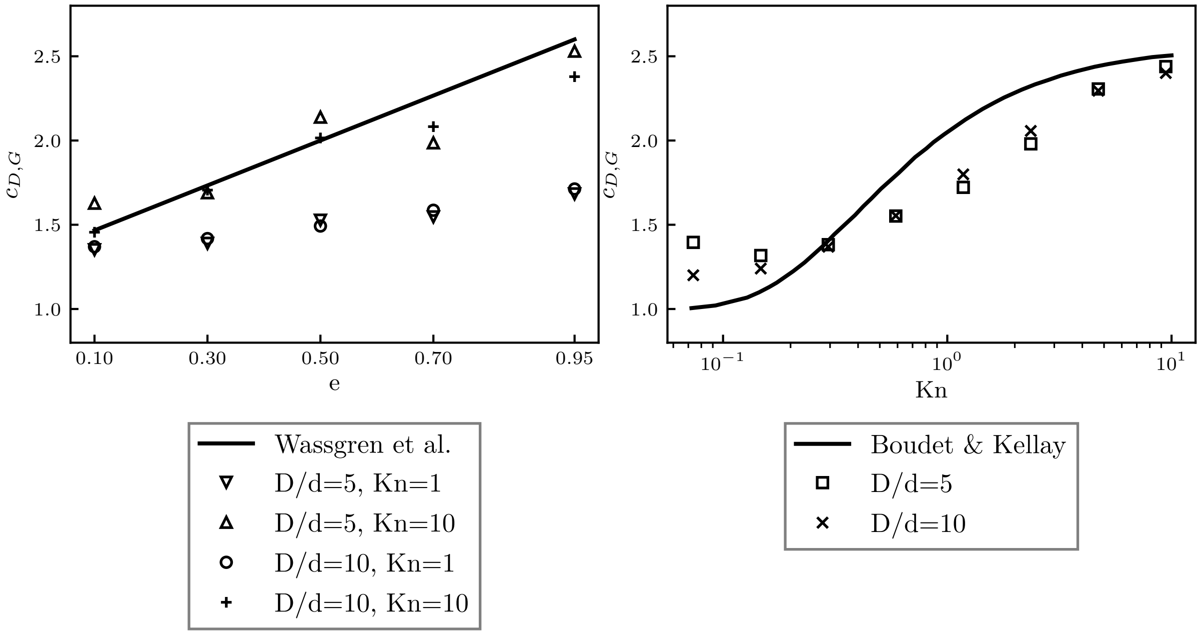

Figure 3: Left: Granular drag coefficient as function of coefficient of restitution e without intersticial fluid (dry granular flow); solid line: prediction by Wassgren et al. [23]. Right: Granular drag coefficient as function of Kn for steel spheres (e=0.93); solid line: best fit of experiments by Boudet & Kellay [22].

Granular drag coefficient depends mainly on the particulate Knudsen number

$$\mathrm{Kn} = \frac{d}{6\sqrt{2}\Theta_\infty D} \tag{23}$$

but also on material properties. The drag coefficient of a cylinder of diameter D experiencing granular flow

$$c_{D,G} = \frac{F_{D,p}}{1/2 \rho_p \Theta_\infty u_\infty^2 (D + d) L_z} \tag{24}$$

is calculated from the drag force $F_{D,p}$, which is made dimensionless by using the particle density ρ_p and diameter d, the upstream solid volume fraction Θ_∞ and velocity u_∞.

Wassgren et al. [23] presented a theoretical derivation of the expected drag coefficient for different coefficients of restitution e. Their prediction for a uniform, non-interacting stream of particles $c_{D,G} = 4\,(e + 1)\,/3$ is depicted in Fig. 3 (left) together with our simulations of frictionless particles. The prediction becomes more accurate as the Knudsen number increases, due to fewer inter-particle collisions taking place. The relation between drag coefficient and Knudsen number has been investigated by Boudet & Kellay [22]. In their experiments, they used an aluminum cylinder in combination with steel spheres ($e = 0.93$), for cylinder to particle diameter ratios $D/d = 27, 110$ and glass beads at $D/d = 92$. The line in Fig. 3 (right) represents their best fit over all experimental results. Our simulations do not follow the curve exactly but show the same trend. Simulations with and without friction did not show much difference. Even though these experiments were conducted with very small particles compared to the cylinder size $d \ll D$, we did not find a significant difference between size ratio 10 and 5 in our computations including friction.

2.4. Wet collision modelling

The particle laden flow conditions of this study are characterized by low impact Stokes numbers of particles onto the cylinder

$$\mathrm{Stk}_{\mathrm{imp}} = \frac{\left(\rho_p + \rho_f/2\right) u_\infty d}{9\mu}, \tag{25}$$

hence fluid drainage before contact has a significant contribution to collisions. Particle interactions are strongly affected by hydrodynamic interaction and lubrication forces, which causes a reduction in the post-collision rebound velocity. Including the calculation of short range hydrodynamic interactions into the algorithm, as discussed in [55], is numerically costly. For the configuration of a particle-laden flow around an obstacle, collisions are likely to occur in front of the cylinder and in shear layers in the wake region, where particles have considerable relative velocities. In front of the cylinder, the collision configuration is close to particle contact at a stagnation point. When approaching an obstacle, the particle motion strongly depends on its size compared to the boundary layer thickness. The dynamics of iso-dense particles in a stagnation point flow has been carefully studied by [56]. The simulation cost for resolving short distance hydrodynamics corresponding to fluid drainage becomes excessively high. Therefore, numerical models have to be employed for coarse grids, which are only able to resolve far-field interactions. The immersed boundary method is supplemented by a hybrid approach including lubrication correction and soft-sphere collision model for the solid contact [57]. The lubrication correction is based on a two-body analytic solution and must be tuned in order to prevent an overestimate of hydrodynamic repulsion (part of the hydrodynamic interaction is already accounted for on the coarse mesh and this effect could be double-counted with the lubrication correction, see [58], [51]). We model the occurrence of wet collisions by using an effective rebound coefficient in the DEM simulations. For our numerical setting, we have chosen a grid discretization $d/\Delta x = 10$ in order to resolve long range hydrodynamics and we make use of effective rebound coefficient for the effect of fluid drainage before solid contact (similarly to [59]).

The effective coefficient of restitution

$$e_{\mathrm{eff}} = e_{\mathrm{dry}} \exp\left(-\frac{\beta}{\mathrm{Stk}_{\mathrm{imp}}}\right), \tag{26}$$

Material	Density $\mathrm{g\,cm^{-3}}$	$e_{\mathrm{dry,p-p}}$	$e_{\mathrm{dry,p-c}}$	$\mu_{\mathrm{s,p-p}}$	$\mu_{\mathrm{d,p-p}}$	$\mu_{\mathrm{s,p-c}}$	$\mu_{\mathrm{d,p-c}}$
Hydrogel	1	0.05	0.1	0.01	0.01	0.5	0.1
Glass	2.5	0.68	0.68	0.9	0.4	0.9	0.4
Iron	7.8	0.4	0.55	1.1	0.15	0.7	0.5

Table 1: DEM material parameters used in this study.

with $\beta = 35$, is calculated [60] from the restitution coefficient without the presence of fluid e_{dry} and the impact Stokes number $\mathrm{Stk}_{\mathrm{imp}}$, which characterizes fluid drainage.

Three different sets of material properties will be utilized that resemble three materials commonly used in experimental suspension flows. Hydrogel particles are iso-dense in water, while glass and iron are considered inertial. The corresponding parameters for the rigid body dynamic solver can be found in Tab. 1.

To test our assumption that wet collisions can be modeled via an effective rebound coefficient, we place a particle of diameter $d/\Delta x = 10$ in a numerical domain that spans 16 diameters in streamwise direction and 6 diameters in cross-stream and spanwise direction. A constant velocity condition $u_{\mathrm{in}} = u_\infty$ is set at the inlet, constant pressure at the outlet and the domain is periodic in the other two spatial directions. The particle is fixed in space and a preliminary simulation is run until the drag force on the particle has converged to make sure that the flow field is steady. Then a second particle is placed in the domain upstream of the fixed particle at a distance of 8 diameters streamwise and half a diameter in cross-stream direction. This moving particle is set to the free-stream velocity $u_p = u_\infty$ such that it will travel downstream and collide with the fixed particle at an oblique angle. We repeat this simulation with three different configurations. First, the dry coefficient of restitution is used for the calculation of collision parameters; secondly, the effective coefficient of restitution is used and finally, the dry coefficient of restitution is used together with the lubrication correction.

The lubrication force is implemented according to Ladd & Verberg [61]:

$$\boldsymbol{F}_{ij}^{lub} = -\frac{6\pi\mu(r_i r_j)^2}{(r_i + r_j)^2}\frac{\boldsymbol{n}}{||\boldsymbol{n}||}u_n\left(\frac{1}{||\boldsymbol{n}|| - r_i - r_j} - \frac{1}{\Delta_c}\right), \tag{27}$$

where r_i, r_j are the radii of sphere i and j, respectively and Δ_c is the cut off distance, at which it is assumed that the hydrodynamic interaction is fully recovered and the lubrication model will be disabled. A value of $\Delta_c = 2/3\Delta x$ is recommended independently of the sphere size. We impose a minimal gap size of $(||\boldsymbol{n}|| - r_i - r_j) = \min(1 \times 10^{-5}, (||\boldsymbol{n}|| - r_i - r_j))$ to avoid exceedingly high repulsive forces.

From Fig. 4, we can evaluate the role of fluid drainage due to lubrication correction before solid contact. There is a net reduction of the particle velocity before the DEM solver for solid contact is operating. Using the effective rebound coefficient provides a good prediction of wet particle collision for a lower CPU cost. Both longitudinal and transverse velocities before and after contact are correctly reproduced without using the lubrication correction which physical effect is accounted for by the effective restitution coefficient which

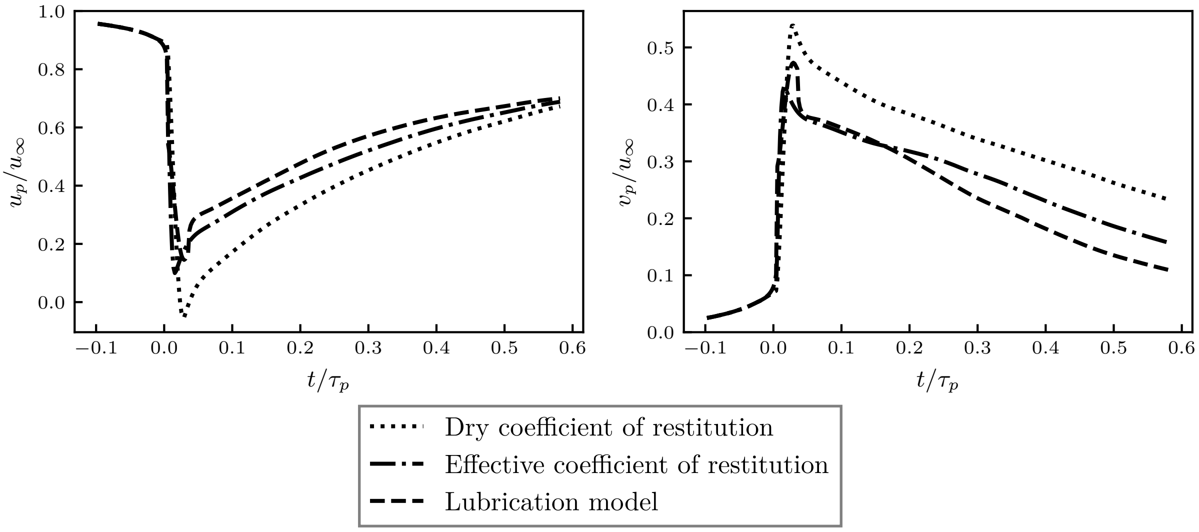

Figure 4: Time evolution of the velocity components (left: streamwise velocity ; right: cross-stream velocity) of a moving iron particle experiencing a collision with a fixed particle. Particle Reynolds number is $\mathrm{Re_p} = 10$, impact Stokes number is $\mathrm{Stk_{imp}} = 9.2$. Dotted line: simulation with the dry restitution coefficient ($e_{\mathrm{dry}} = 0.4$). Dashed line: simulation with dry restitution coefficient and lubrication correction. Dot-dashed line: simulation with the effective restitution coefficient ($e_{\mathrm{eff}} = 0.009$) and no lubrication.

depends on the impact Stokes number.

2.5. Numerical settings

The cylinder has length L_y, the uniform inlet velocity is equal to the upstream velocity $u_{in} = u_\infty$ and the fluid has density ρ_f. The simulation domain size spans 40 cylinder diameters in streamwise direction, 24 cross-stream, and 5 spanwise.

Four physical parameters from the classical, single phase von Kármán vortex street are extracted and used to validate our computational methods. The vortex shedding frequency f is characterized by the

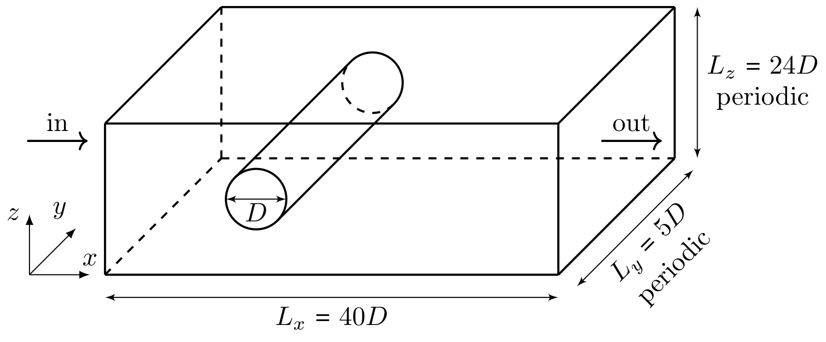

Figure 5: Schematic presentation of the simulation domain.

Re	c_D	L_r/D
20	2.134	0.94
50	1.45	2.92
100	1.123	6.08
150	0.979	9.14

Table 2: Steady single phase cylinder flow parameters from our simulations (see Fig. 6 for validation with data from literature).

Strouhal number

$$\mathrm{St} = \frac{fD}{u_\infty}, \tag{28}$$

fluid drag F_D and lift F_L forces are reduced to the dimensionless coefficients

$$c_D = \frac{F_D}{(1/2)\,\rho_f u_\infty^2 D L_z} \tag{29}$$

and

$$c_L = \frac{F_L}{(1/2)\,\rho_f u_\infty^2 D L_z}, \tag{30}$$

respectively. The recirculation length L_r is defined as the streamwise extent of the region behind the cylinder, in which the fluid flows upstream. It is computed from the time averaged flow field and normalized by the cylinder diameter D. We employ the single relaxation time model (BGK) for the suspension flow around a cylinder because it provides sufficiently good results and is computationally faster. The simulation results we obtained are documented in Tab. 2, 3 and a comparison with reference experiments and numerical computations is found in Fig. 6. Our simulation results are in very good agreement with reference data from literature. The Strouhal number is slightly above the reference data due to the staircase shape of the cylinder imposed by the LBM discretization but the discrepancy is always below 1%. The mean recirculation length is adequately reproduced by our simulations. Simulations are started with a steady flow and it takes some time for the velocity perturbation to grow in the linear regime before the onset of wake instability yielding vortex shedding. Information on the steady recirculation length is gathered for each Reynolds number (although above the threshold of vortex shedding) by measuring the wake length before the oscillatory instability sets in. The same procedure is used to measure the drag coefficient before vortex shedding (steady flow) and after wake instability (unsteady flow). Our simulations results stand among the literature data in Fig. 6, top right panel.

Particles are seeded at the domain inlet at random locations with the same velocity as the surrounding fluid u_{in}. The number of particles seeded per time step is

$$\dot{n} = \frac{u_{\mathrm{in}} \Theta A}{V_p}, \tag{31}$$

where $A = L_y L_z$ is the cross section area and $V_p = \pi d^3/6$ is the particle volume, is set in order to achieve the desired solid volume fraction Θ . The domain is periodic in cross-stream ($\mathbf{z}$) and spanwise ($\mathbf{y}$) directions and

Re	St	c_D	$c_{L,\mathrm{RMS}}$	L_r/D
50	0.127	1.489	0.045	2.42
60	0.139	1.451	0.100	2.04
80	0.156	1.401	0.177	1.64
100	0.168	1.374	0.241	1.40
150	0.187	1.357	0.382	1.04

Table 3: Unsteady single phase cylinder flow parameters from our simulations (see Fig. 6 for validation with data from literature).

a constant pressure boundary condition is applied on the outlet to mimic a free exit of fluid. Non-reflective boundary conditions are not required because under current flow conditions, vortices leaving the domain are not expected to be strong enough to cause stability problems or unphysical behavior. Particles will be removed from the computation when their volume is entirely outside of the fluid domain. The fixed cylinder is always assigned the properties of glass material.

The initial transient of the simulation is assumed to be completed once drag force, lift force RMS and recirculation length have reached a constant average value. From then, temporal signals and mean flow fields are recorded for 20 periods of the expected vortex shedding oscillation. The instantaneous fluid velocity is recorded at three points that are located one diameter in cross-stream ($\mathbf{z}$) and 1, 5, 20 diameters in streamwise ($\mathbf{x}$) direction away from the cylinder center in order to evaluate the vortex shedding frequency through fast Fourier transform. This is an unambiguous procedure for single phase flows since there is one distinct shedding frequency, but the introduction of particles creates noise in the velocity spectrum. At flow states close to the bifurcation, it becomes difficult to decide whether or not a flow is unsteady. We declare a configuration to be unsteady if we can find one distinct peak in the frequency spectrum which amplitude is at least twice more than the other peaks.

For accuracy reasons we want particles to be resolved with at least 10 $d/\Delta \mathrm{x}$, so to achieve a ratio of $D/d = 5$ the cylinder needs to have 50 cells per diameter. The dimensionless frequency of particle oscillation due to vortex shedding in the wake of the cylinder can be estimated as $\psi^2 = 2\pi \, \mathrm{Stk} \, \mathrm{Re} \, (d/D)^2$ which ranges from 1 to 5 for $D/d = 5$ and is always below 1.25 when $D/d = 10$. To ensure that the boundary conditions have no influence on simulation results, the domain size in each spatial direction has been varied to find the dimensions at which global flow parameters remain constant. The effects of the size of the simulation domain and the spatial discretization have been tested on a reference case of particle laden flow (see Tab. 4). We observe less than 1% variations of the Strouhal number or the drag and lift coefficients.

The numerical setup allows accurate results while keeping the simulation cost adequate to run on supercomputing facilities. The code used for this study is waLBerla [62], an open-source C++ multiphysics software framework (more validations on particulate flows are available in [63]). It can be used as a toolbox

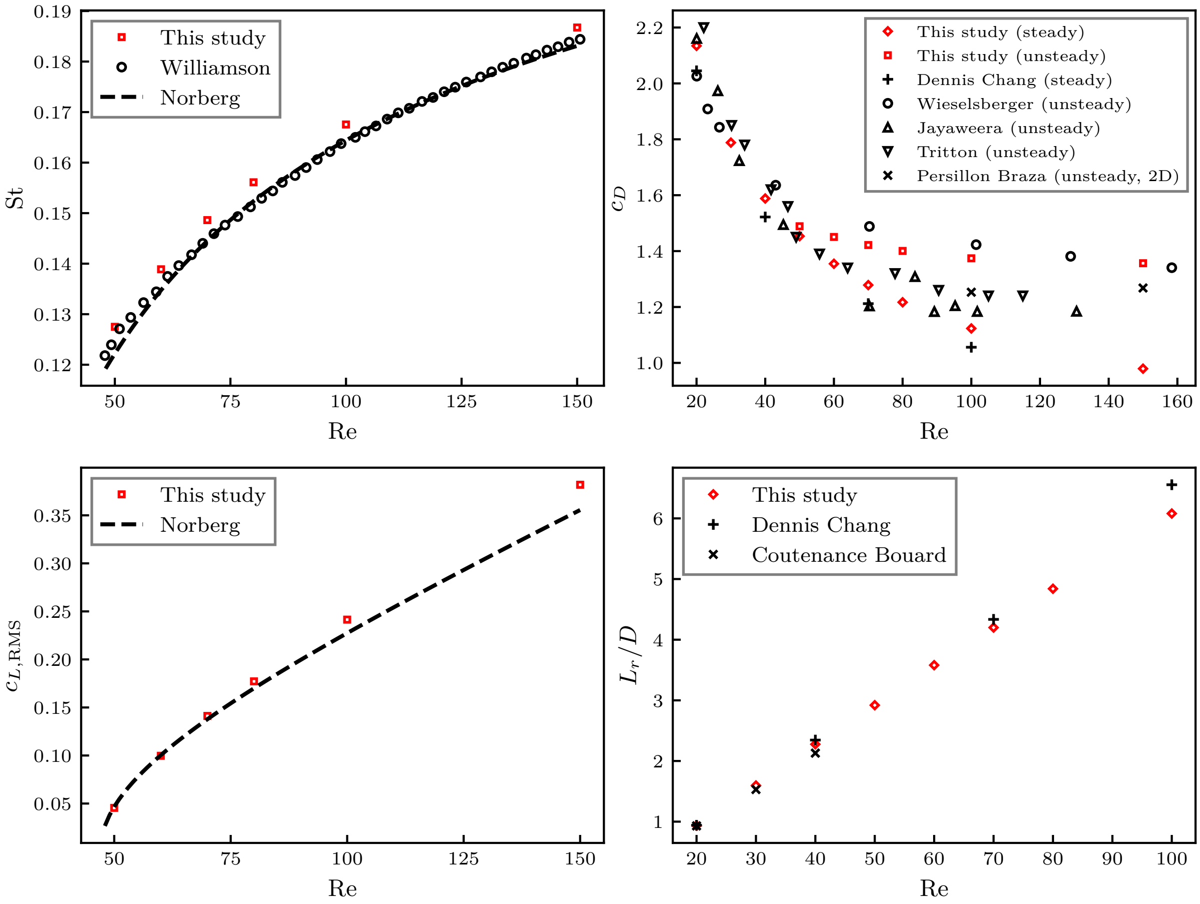

Figure 6: Single phase flow past a circular cylinder: Top/left - Dimensionless vortex shedding frequency; top/right - drag coefficient; bottom/left - R.M.S. of lift coefficient; bottom/right - wake recirculation length under steady regime.

for designing various types of applications such as LBM computations [64]. waLBerla was designed from the ground up for high-performance computing on massively parallel clusters [65]. The framework is based on a block-structured domain partitioning in order to achieve extreme scalability and node level performance [66]. The total number of lattice cells amounts to 600M and at the highest solid volume fraction of 20% there are more than 220,000 particles simultaneously resolved inside the domain.

The computational speed of LBM algorithms is typically measured in Million Lattice Updates Per Second (MLUPS) i.e., the number of cell updates every second. For single phase, we achieve 5620 MLUPS on 600 cores with *Intel Cascade Lake 6248* architecture of the *Jean Zay* supercomputer [67]. When introducing Lagrangian particles into the domain, the algorithm has to treat collisions, particles boundary conditions and refill missing distribution functions which slows down the performance to 1580 MLUPS at 20% volume fraction. To complete a typical simulation of 200,000 time steps, corresponding to a size ratio $D/d = 5$, a total of 3660 (resp, 13030) CPU hours are required at $\Theta = 0\%$ (resp., 20%). The relation between

L_x/D	L_y/D	d/Δ_x	St	c_D	$c_{L,\mathrm{RMS}}$
40	24	10	0.1401	1.392	0.100
80	24	10	0.1401	1.386	0.098
40	48	10	0.1401	1.383	0.099
40	24	15	0.1417	1.396	0.099

Table 4: Effect of domain size and mesh discretization for particle-laden flow properties. The fluid Reynolds number is Re = 80 and the volume concentration of iso-dense particles ($D/d = 5$) is $\Theta = 10\%$.

particle volume fraction and computational speed is depicted in Fig. 7. These numbers do not include post processing routines. The number of lattice cells for simulations at size ratio $D/d = 10$ amounts to 4,800M with over 1.76 million of particles inside the computational domain at 20% solid volume fraction. These larger computations were performed on the *OCCIGEN* supercomputer [68] with *Intel Haswell E5-2690V3* architecture using 4,800 cores.

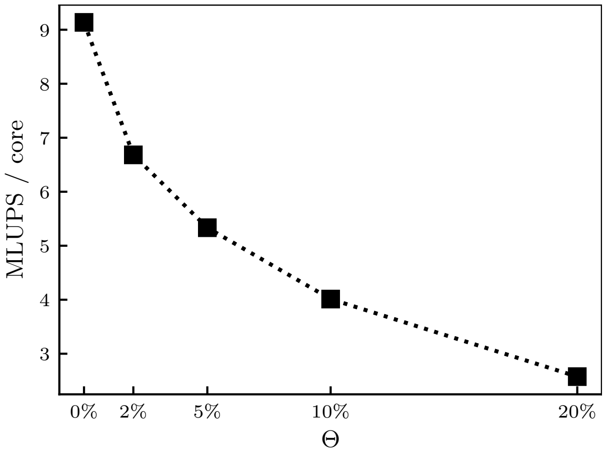

Figure 7: Computational performance measured in MLUPS per core utilized for an increasing number of particles inside the domain.

3. Results

3.1. *Iso-dense particles (hydrogel)*

By introducing rigid spherical particles into the fluid, a specific response of the flow is expected relative to the solid volume concentration. A simple model of particle induced flow modification is based on the concept of effective physical properties for the mixture. The stiffness of particles allows them to resist compression and elongation generating hydrodynamic perturbations in the flow field which dissipate additional energy. At higher volume fraction, particle interactions such as lubrication effects and solid contact come into play. Close to maximum solid packing volume fraction, hydrodynamic stresses are dominated by friction forces.

As we investigate flow up to 20% volume concentration, this will not be the case for this study, except possibly for very localized regions in the vicinity of the cylinder. There is a number of correlations for estimating the effective suspension viscosity, namely Einstein [69], Batchelor & Green [70], Dougherty & Krieger [71], Hsueh & Becher [72], Eilers [73]. For this study we employ Eilers' equation with $\Theta_{\max} = 0.64$ corresponding to random assembly of spheres at close packing density

$$\mu_{\text{eff}} = \mu_0 \left(1 + \frac{2.5\Theta}{2(1 - \Theta/\Theta_{\max})}\right)^2 . \tag{32}$$

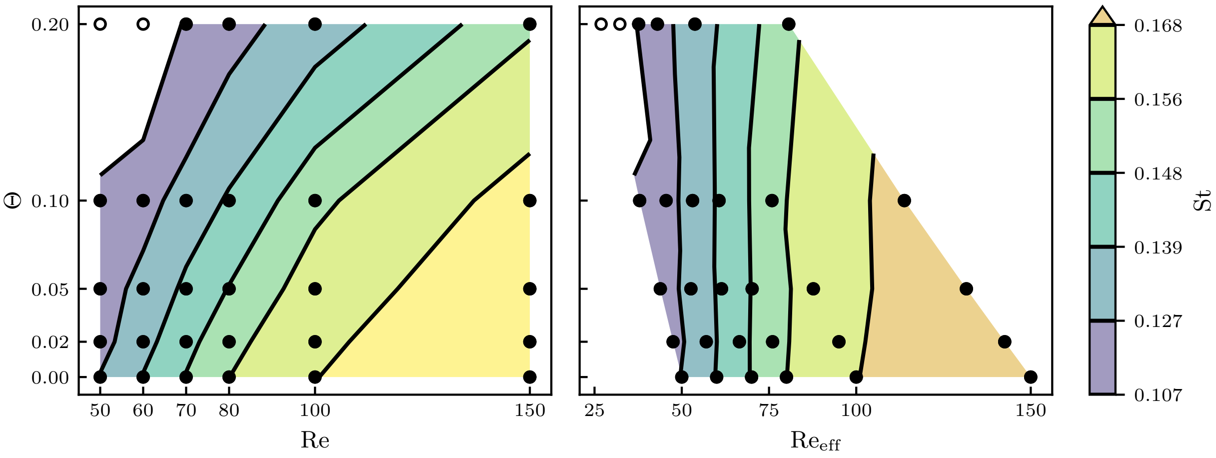

Figure 8: Dimensionless shedding frequency (Strouhal number) as function of Re, Θ. Closed symbols: unsteady flow; open symbols: steady flow.

The dimensionless shedding frequency St is represented as color map over the flow Reynolds number Re and solid volume fraction Θ in Fig. 8. Filled symbols indicate unsteady flow states and possibly vortex shedding, whereas open symbols and white area represent steady flow states. When increasing the particle volume fraction, the effective suspension viscosity increases causing flow oscillations to reduce. When accounting for the suspension viscosity by using an effective Reynolds number $\text{Re}_{\text{eff}} = \frac{\rho_f u_\infty L}{\mu_{\text{eff}}}$, the contour lines of St become vertical indicating similar flow states for constant Re_{eff}, corresponding to the behavior of an equivalent fluid. When all data are gathered on a single plot, they collapse onto a master curve matching the single phase flow results in Fig. 9 using the effective viscosity of the suspension. This shows that the major role of finite-size iso-dense particles is to enhance viscous damping due to non-deformability of solid particles in regions of high strain rate.

For the single phase flow the transition between steady and unsteady flow is marked by the critical Reynolds number $\text{Re}_{\text{crit}}(\Theta = 0) \approx 48$. The presence of particles triggers instabilities in the flow field, which is why we can find flow unsteadiness at sub-critical Reynolds numbers $\text{Re}_{\text{eff}} < \text{Re}_{\text{crit}}(\Theta = 0)$. These flows oscillate at lower frequency than the minimum vortex shedding frequency found in single phase flows $\text{St} < \text{St}(\Theta = 0, \text{Re} = \text{Re}_{\text{crit}})$, but the cylinder is not necessarily shedding vortices. Local vorticity production at the

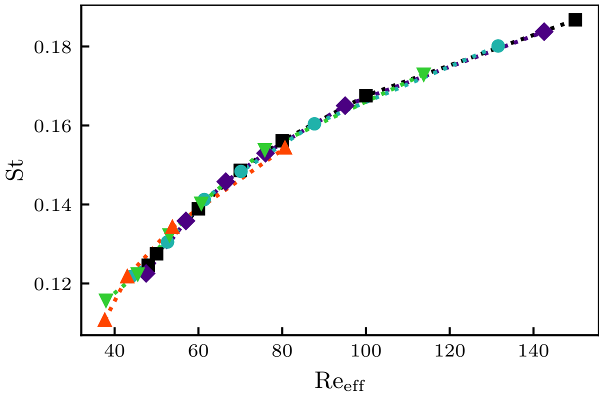

Figure 9: Strouhal number as function of $\mathrm{Re}_{\mathrm{eff}}$ for various volume concentrations Θ in colored symbols. Filled black squares stand for single phase flow.

top and bottom of the cylinder is not intense enough for the Kelvin-Helmholtz instability of the shear layer to set in. The wake is weakly meandering periodically without occurrence of roll-up that yields alternative vortex shedding typically observed in the von-Karman street. At Reynolds numbers $\mathrm{Re}_{\mathrm{eff}} > \mathrm{Re}_{\mathrm{crit}}(\Theta = 0)$ the classic vortex shedding is observed again.

In the unsteady regime, the averaged recirculation zone is shrinking as vortex shedding intensifies. The evolution of recirculation length for different Re and Θ is shown in Fig. 10. Due to the effect of effective viscosity a suspension can return to steady flow, which causes wake length to follow the trend seen in Fig. 6. When transforming the plot to effective parameters, all lines collapse onto a mastercurve that follows the steady single phase evolution up to $\mathrm{Re}_{\mathrm{crit}}$ and the unsteady single phase curve beyond. Haddidi et al. [31] have shown a depletion of particles in the recirculating wake for Reynolds numbers well below the onset of unsteadiness. We can observe a similar behavior in our simulations at $\mathrm{Re} = 50$, where the concentration of particles in the wake is low. Simulations of iso-dense particles in a confined channel using a suspension balance direct-forcing immersed boundary model (SB-FD-IBM) by Dbouk [74] also yield a depletion of particles in the wake region, which is in agreement with our results. In their configuration, the onset of vortex shedding in terms of Reynolds number is delayed due to the confinement by the walls. In contrast to our approach the vortices are void of particles in their Eulerian simulations. This behavior indicates that particle-particle interactions play an important role in transporting finite size particles towards the vortex center for unsteady regime.

Using effective viscosity collapses all the simulation results onto the single phase flow evolution for cylinder drag and lift coefficients. Fig. 11 reveals a slight drag underprediction for high solid volume fraction as well as high Reynolds numbers. For suspensions below $\mathrm{Re}_{\mathrm{crit}}$, the single phase lift coefficient RMS is equal to zero but nonzero fluctuations are found in the signal for two-phase flows due to the random collisions of particles on the surface of the cylinder. A rolling average with window length of $T/10$ corresponding to the period T of minimum Strouhal number $\mathrm{St}_{\mathrm{min}} = 0.12$ was applied to smooth out random fluctuations.

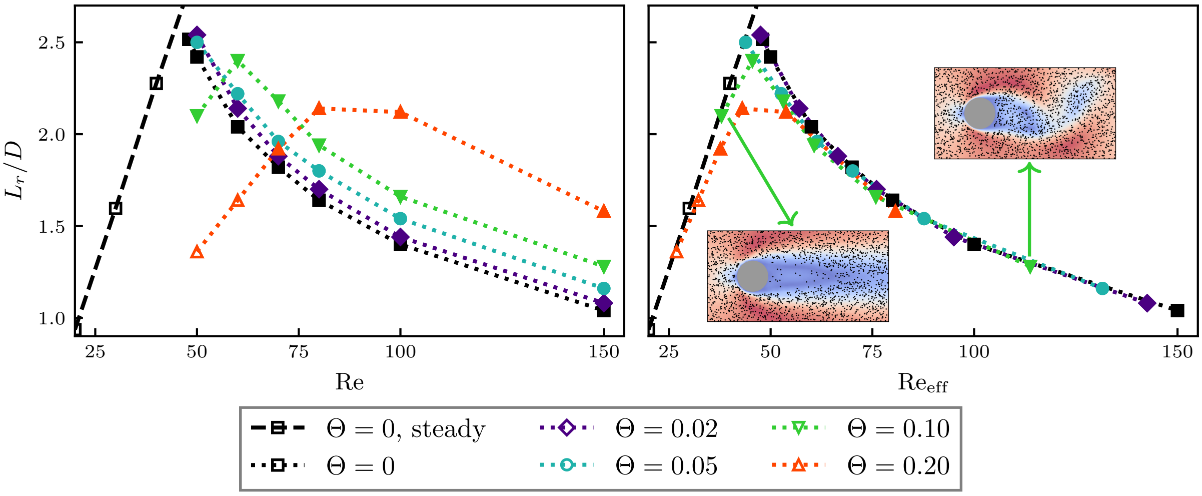

Figure 10: Recirculation length as function of Re. Closed symbols: unsteady flow; open symbols: steady flow. Instantaneous flow snapshots at $\Theta = 10\%$ and $\mathrm{Re_{eff}} = 38, 114$ colored by fluid velocity magnitude and particles are represented as black points. Point size is not representative of actual particle size.

The effective viscosity correlation used here is derived from experiments of suspensions with small particle diameter compared to the cylinder $d \ll D$. It was not obvious that they can hold true for a diameter ratio of $D/d = 5$. To investigate the effect of particle size, we double the cylinder and domain sizes but keep the previous particle diameter to achieve $D/d = 10$ while maintaining the particle resolution of 10 lattice cells per diameter. As shown in Fig. 12, the drag coefficient remains unchanged. However, the recirculation length evolution is closer to the single phase flow data in the region close to the onset of unsteady flow.

3.2. Glass particles

The material we investigate now is composed of glass particles, which have a relative density $\rho^* = \rho_p/\rho_f = 2.5$. Increasing the material density means particles will have more inertia and less tendency to follow the flow streamlines when approaching the cylinder. We recall that gravity is not considered. The effect of inertia is not accounted for in the effective viscosity model and can have an impact on the flow rheology, especially in the wake zone and in high shear stress regions at top and bottom of the cylinder. Contour lines of the dimensionless shedding frequency in Fig. 13 reveal a slight inclination to higher $\mathrm{Re_{eff}}$ at increasing volume fraction. Similarly to hydrogel, there is a sub-critical region where the flow is unsteady but not shedding vortices. Other quantities like drag and lift coefficients, recirculation zone length abide to the predicted collapse on the single phase curve, except for points at the higher Reynolds numbers, which show a slight deviation. It should be noted that the Reynolds number $\mathrm{Re_{eff}} = \frac{\rho_{\mathrm{eff}} u_\infty L}{\mu_{\mathrm{eff}}}$, as well as the drag and lift coefficient $c_{\mathrm{eff}} = \frac{F}{\rho_{\mathrm{eff}} u_\infty^2 A/2}$, now have to incorporate the suspension's effective density $\rho_{\mathrm{eff}} = (1-\Theta)\rho_f + \Theta\rho_p$ which is different from fluid density and evolves with particle volume concentration.

Glass has similar density than sand and all features we observed in our simulations are relevant to

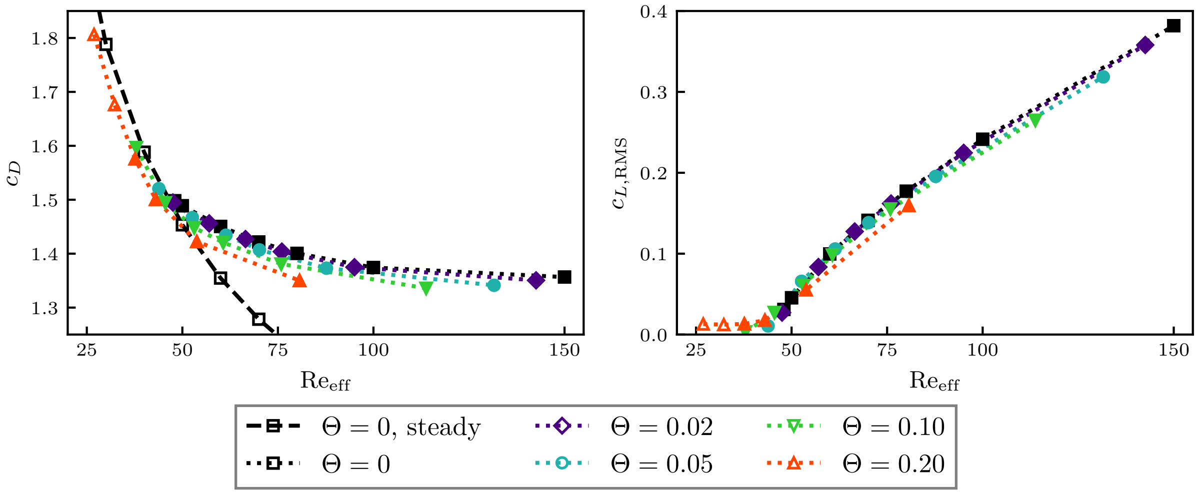

Figure 11: Drag and lift RMS coefficients as function of Re. Closed symbols: unsteady flow; open symbols: steady flow.

sediment transport in water. Inertia starts to come into play while effective density reaches 1.3 for volume fraction $\Theta = 20\%$. This leads to slight discrepancy between the particle resolved simulations and mode prediction for the effective mixture.

3.3. Iron particles

At even higher relative density of $\rho^* = 7.8$ we observe the failure of effective viscosity modeling due to significant inertia effect. Strouhal contour lines are heavily skewed with many simulations at high volume fraction showing flow oscillations without vortex shedding or with vortices developing further downstream, as we will see later. Suspension drag coefficients in the supposedly unsteady regime are deviating away from the single phase unsteady curve towards the steady curve. This response is due to the increased inertia of particles, which deviates particle trajectories from fluid streamlines and inhibits the flow from developing its inherent flow structure. Similar to Fig. 14, suspension recirculation length above $\mathrm{Re}_{\mathrm{eff}} = \mathrm{Re}_{\mathrm{crit}}(\Theta = 0)$ is drifting away from the single phase unsteady curve and is approaching the steady curve. Lift RMS is strongly dampened compared to single phase unsteady flow highlighting the damping of vortex shedding.

In this regime, particles impact the cylinder with significant momentum. The Stokes number characterizing the particles is now sufficiently large to prevent the particles from following the fluid elements and the wake region remains depleted of particles. This is consistent with the simulation results of [32] which showed that when particle inertia is increased the limit cycle of particle trajectories in the wake region becomes unstable. Although those simulations were carried out for a single particle, here we observed the same response of the particle laden flow for many particles interacting in the wake region.

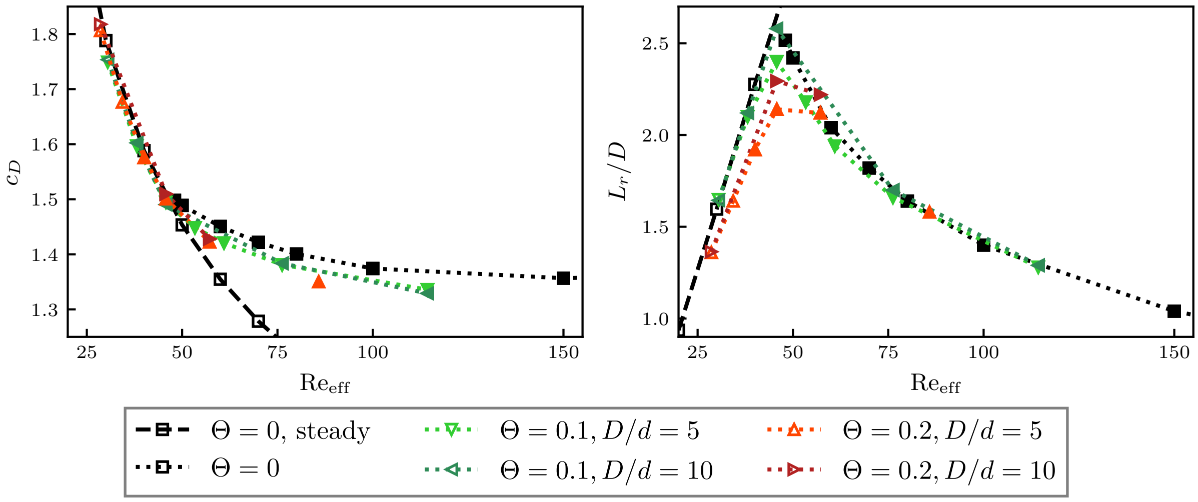

Figure 12: Drag and recirculation length as function of Re. Comparing particle sizes D/d=5 and D/d=10. Closed symbols: unsteady flow; open symbols: steady flow.

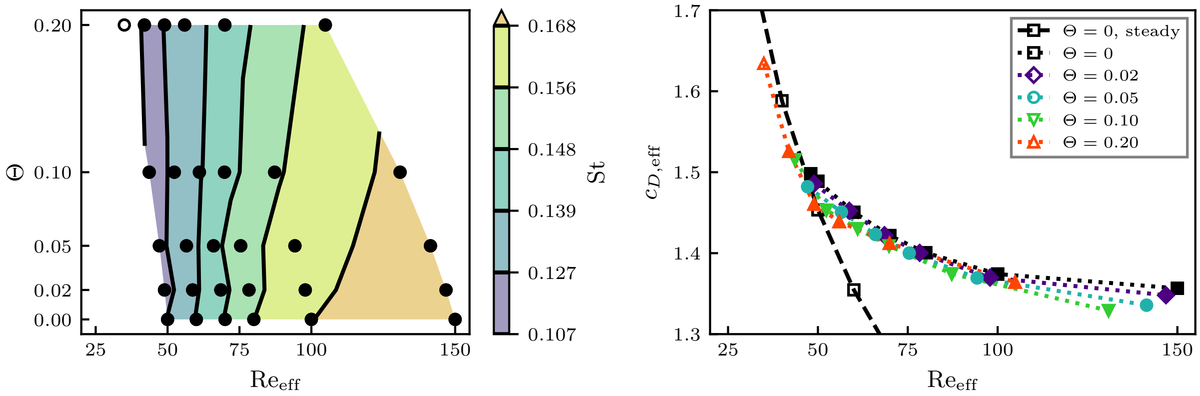

Figure 13: Strouhal number and drag coefficient of a suspension with glass particles. Closed symbols: unsteady flow; open symbols: steady flow.

4. Discussion of contributions to the drag force

The reliability of effective fluid prediction for the three different materials is summarized in Fig. 15 by relating the suspension drag coefficient to its single phase value at corresponding $\mathrm{Re}_{\mathrm{eff}}$. If the suspension is unsteady - even if it is not vortex shedding - we relate it to the unsteady single phase drag, otherwise we compare it to the steady drag coefficient. Hydrogel and glass suspensions are close to the ideal line, where the model prediction matches the suspension drag exactly. However, with iron particles there is an overestimate for steady cases and an underestimate for unsteady cases.

From our simulations, we can extract separately the contribution to the drag force which is exerted by the fluid phase and the rest which is caused by particle collisions transferring momentum to the cylinder. We added another suspension material with particles of relative density $\rho^* = 100$ to approach if it approaches

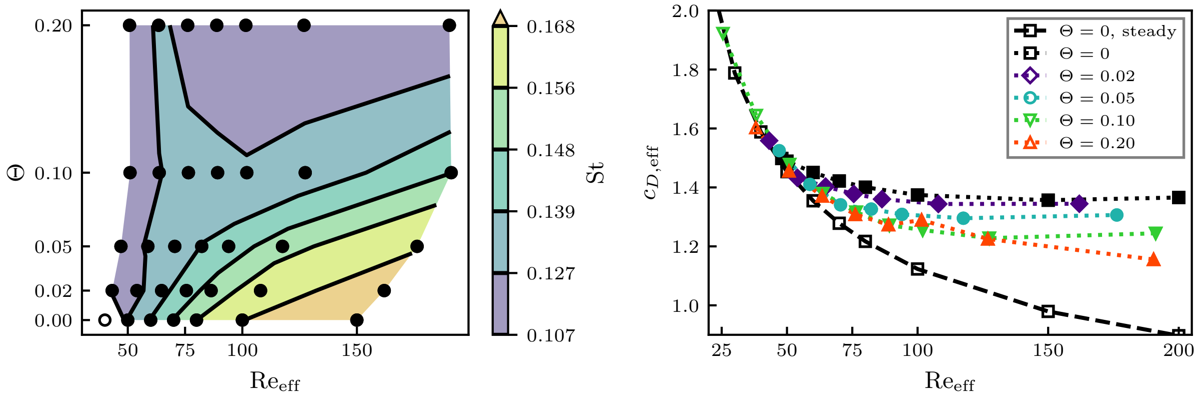

Figure 14: Strouhal number and drag coefficient of a suspension with iron particles. Closed symbols: unsteady flow; open symbols: steady flow.

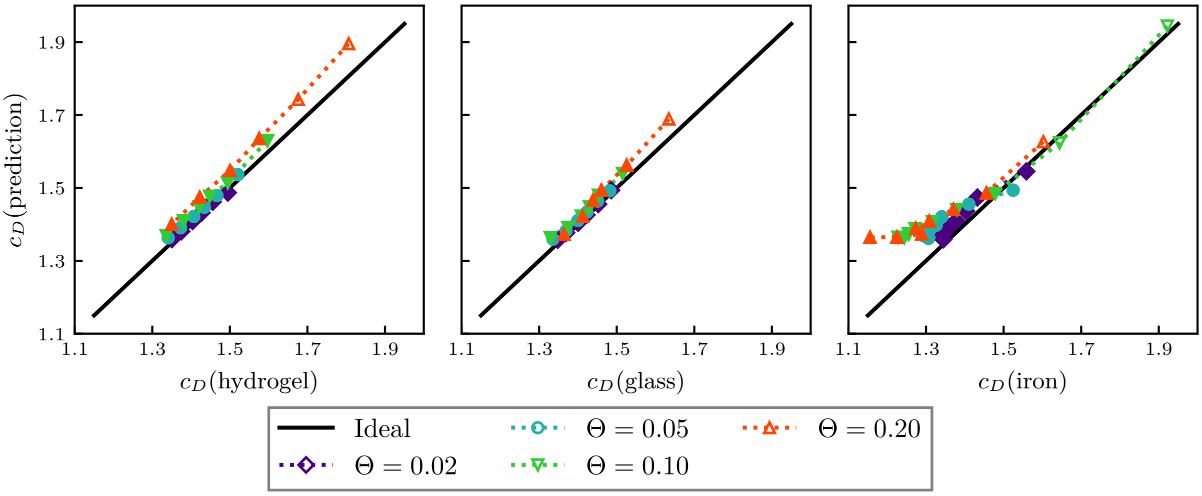

Figure 15: Suspension drag coefficient compared to equivalent fluid prediction. Closed symbols: unsteady flow; open symbols: steady flow.

the response of a granular flow in a gas $(\rho^* \gg 1)$. Fig. 16 shows the suspension's particle contribution as a granular coefficient, revisiting eq. (24). Increasing the relative density brings the drag particle contribution closer to a dry granular flow. At high Reynolds number the effect of fluid viscosity is low, thus the fluid has less resistance against particles and more of their momentum is being transferred onto the cylinder through collisions. This is especially true for the case of iron and $\rho^* = 100$ but opposite for hydrogel. Additionally, the particle contribution at high density ratios follows the trend of increased drag at high Knudsen number, whereas hydrogel suspension shows the opposite trend. There are two main distinctions in the flow structure that can be made responsible for these observations. One is that low density ratio suspensions are more easily prone to unsteady vortex shedding while particles are following fluid pathlines and the other one is the formation of a bow shock, typically observed for granular flows at high solid volume fraction. The occurrence of bow shock in front of the cylinder points out the strong decorrelation of fluid and particles motion in the wake. The bow shock is formed due to the rebound of particles on the curved shape of the cylinder. Particle trajectories are deflected and progressively entrained by the fluid stream (the entrainment rate is controlled by the particle Stokes number).

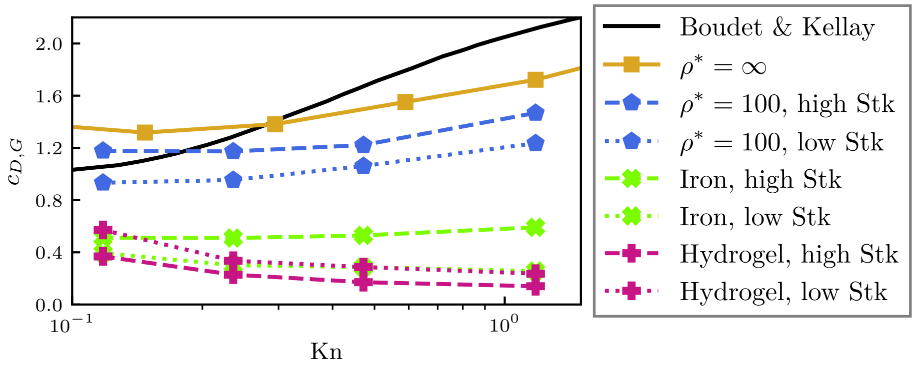

Figure 16: Contribution to the drag of particle collisions for different suspensions compared to granular drag coefficient.

Finally we give an overview on the ratio between fluid $c_{D,f,\mathrm{sus}}$ and solid $c_{D,p,\mathrm{sus}}$ drag contributions of suspensions with different materials and how they compare to the equivalent single phase fluid or granular flow respectively. The particle contribution $c_{D,p,\mathrm{sus}}$ in Fig. 17 is small for iso-dense particles but grows with increasing density ratios. As particle inertia increases, the impact Stokes number increases and yields stronger momentum transfer through collisions in front of the cylinder. For suspensions of hydrogel and glass particles, the drag coefficient is equal to the single phase $c_{D,\mathrm{sp}}$ at corresponding effective Reynolds number. The same estimate is valid for iron but only in the steady regime. When $\mathrm{Re}_{\mathrm{eff}} > \mathrm{Re}_{\mathrm{crit}}(\Theta = 0)$ a suspension of iron particles can neither be described as an effective single phase steady nor unsteady flow, nor as granular media. At high density ratios the particle influence on the drag force dominates, but the fluid part cannot be neglected. The equivalent fluid model is no longer applicable, instead the suspension drag is approximately equal to the pure granular drag $c_{D,g}$.

The observations on the drag also manifest in the local distribution of particles in the instantaneous flow field, showed in Fig. 18. The fluid viscosity is kept constant while the density ratio changes, leading to different Stokes numbers $\mathrm{Stk} = \frac{\tau_p u_\infty}{D}$ with $\tau_p = \frac{(\rho_p+\rho_f/2)d^2}{18\mu_f}$. This definition of the particle relaxation time accounts for particle inertia and added-mass effect but assumes Stokes drag force acting on the particles. In our case, the slip velocity is at maximum 20% of the mean flow velocity Fig. 21 yielding a maximum particle Reynolds number of 6. For most of our simulation cases, the particle Reynolds number is below 1 and Stokes drag is a good estimate for the particle relaxation time.

We can identify four unique flow states. Hydrogel particles are uniformly distributed throughout the flow, even in vortex regions. On the other hand, glass particles at Stk = 1 yield vortices depleted of particles. For low Stokes numbers Stk ≤ 1 no bow shock is present. For the heavier iron particles we observe that

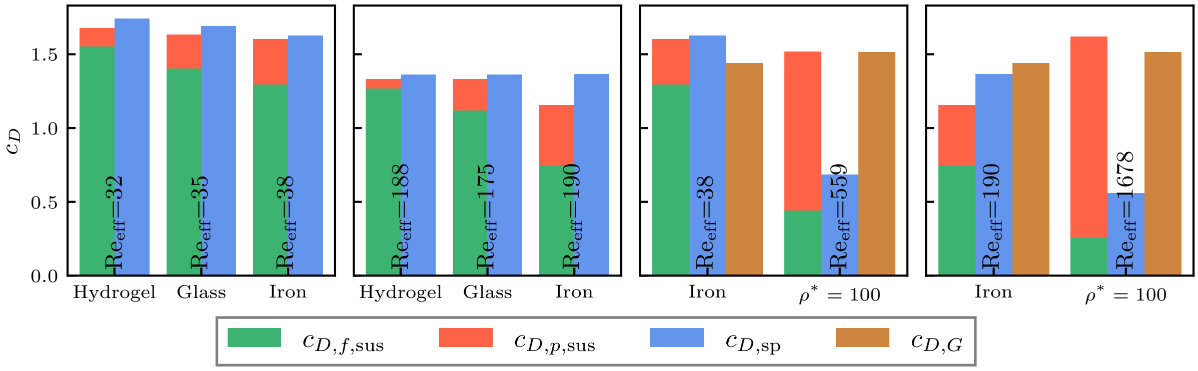

Figure 17: Fluid $c_{D,f,\mathrm{sus}}$ and particle $c_{D,p,\mathrm{sus}}$ contributions to suspension drag coefficient compared to single phase drag $c_{D,\mathrm{sp}}$, granular drag $c_{D,g}$. All values are taken from suspensions with $\Theta_\infty = 20\%$ solid volume. Single phase drag coefficient at Re > 200 is an extrapolation from obtained simulation results.

vortex shedding is spatially delayed downstream due to the formation of a weak bow shock. The wake region and vortices are largely depleted of particles. When the Stokes number increases further to Stk > 10, the wake is completely free of particles and an apparent bow shock is visible similar to dry granular flow. Vortex shedding is stalled or delayed so far that it is outside of the simulation domain.

Shi et al. [29] conducted numerical studies of one-way coupled particle laden flows around a cylinder for high density ratios $\rho^* = 1000$ and low volume fraction $\Theta = 10^{-6}$. The bow shock observed in their simulations is wider than ours and fluid vortex shedding is not inhibited by particle inertia, since the fluid is not influenced by the presence of particles (one-way coupling simulations which are unphysical at moderate particle concentration). Similarly the results of Luo et al. [30] show unsteady vortex shedding for Stokes numbers up to 100. They examined dilute flows with high density ratios and a one-way fluid-particle coupling, where only Stokes drag force is considered. In agreement with our results, there is a depletion of particles in vortex regions and an extended recirculation zone for Stk > 1. The work of Jalali [24] contains snapshots of computations from granular flows that show a bow shock comparable to the one in our simulation involving high-density particles.

5. Eulerian statistics of particle-laden flows

Averages of Eulerian quantities were formed after the transient period to reach steady or periodic regimes. Fig. 19 shows the fields of mean fluid velocity for particle laden flows with hydrogel and iron particles at two different effective Reynolds numbers. While the flow fields look similar at $\mathrm{Re_{eff}} = 30$ for the two different materials, there is a clear difference at $\mathrm{Re_{eff}} = 80$. With hydrogel the wake region is oscillating at $\mathrm{Re_{eff}} = 80$, leading to vortex shedding which on average corresponds to a shorter mean length of the recirculation region. With iron particles which are more inertial the flow instability is suppressed and the wake remains steady yielding a small increase of the recirculation zone.

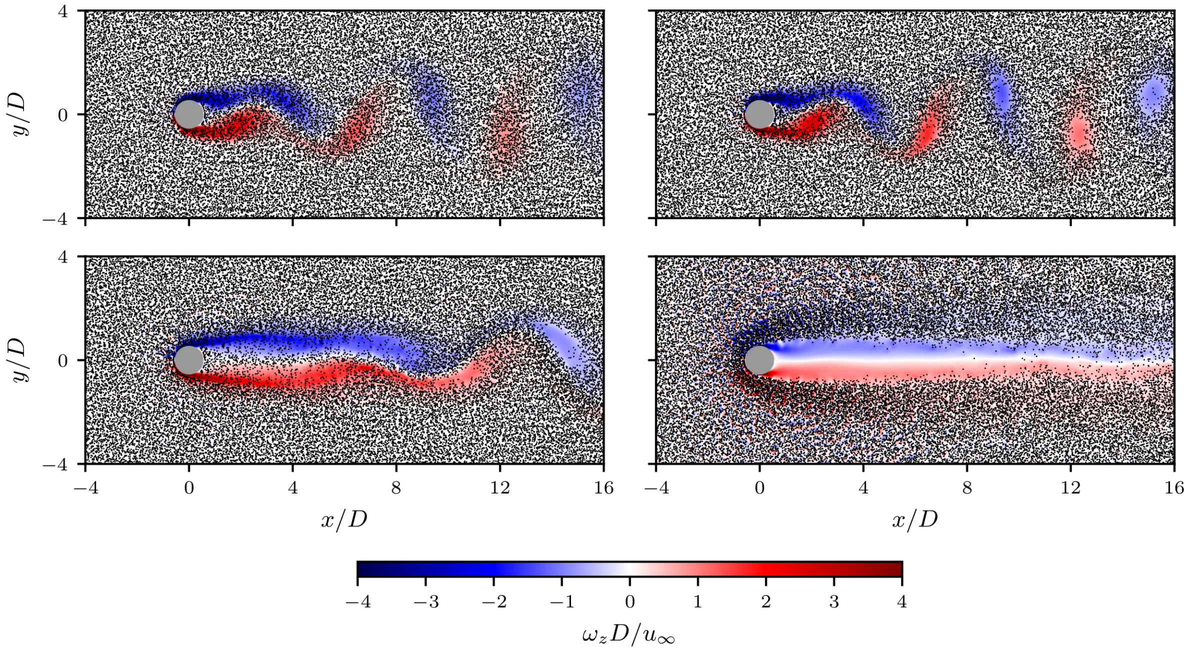

Figure 18: Snapshot of particle positions and vorticity field at constant volume fraction $\Theta_\infty = 20\%$ and fluid Reynolds number Re = 150. Hydrogel (Stk = 0.5): top/left; Glass (Stk = 1): top/right; Iron (Stk = 2.8): bottom/left; $\rho^* = 100$ (Stk = 33.5): bottom/right.

Time averaged spatial distributions of the particle concentration are presented in Fig. 20 and relative velocity between particles and fluid are shown in Fig. 21. When interpreting the global response of the particulate flow in terms of effective viscosity, the underlying assumption is that the effective suspension viscosity is uniform throughout the flow. However, the effective viscosity is depending on the local particle concentration, which is non-uniform (Fig. 20). There is an accumulation of particles near the stagnation point in front of the cylinder and a lower concentration in the recirculation zone. The accumulation in front plays a major role on the effective flow features because this region is characterized by both large strain rate and larger particle concentration, therefore larger viscous damping. We observe an increased particle volume fraction along the edges of the recirculation zone for the non-oscillating wake (Fig. 20 left), whereas the recirculation zone is shortened for the oscillating wake (Fig. 20 top, right). For a suspension with hydrogel particles at $\mathrm{Re}_{\mathrm{eff}} = 80$, we find an accumulation of particles that are stuck right behind the cylinder. The spiralling motion of particles inside the wake at $\mathrm{Re}_{\mathrm{eff}} = 30$ transports particles outwards towards the limit cycle [32]. On the other hand, flow oscillations at $\mathrm{Re}_{\mathrm{eff}} = 80$ and particle collisions in presence of shear layers at the edge of the wake can cause particles to enter the recirculation zone. These two mechanisms are prominent for low particle inertia. At high particle inertia (Fig. 20 bottom), the bow shock is clearly visible and its influence increases at high Reynolds numbers corresponding also to high particle Stokes number. The particle depleted region extends simultaneously and particle and fluid are loosely coupled after cylinder

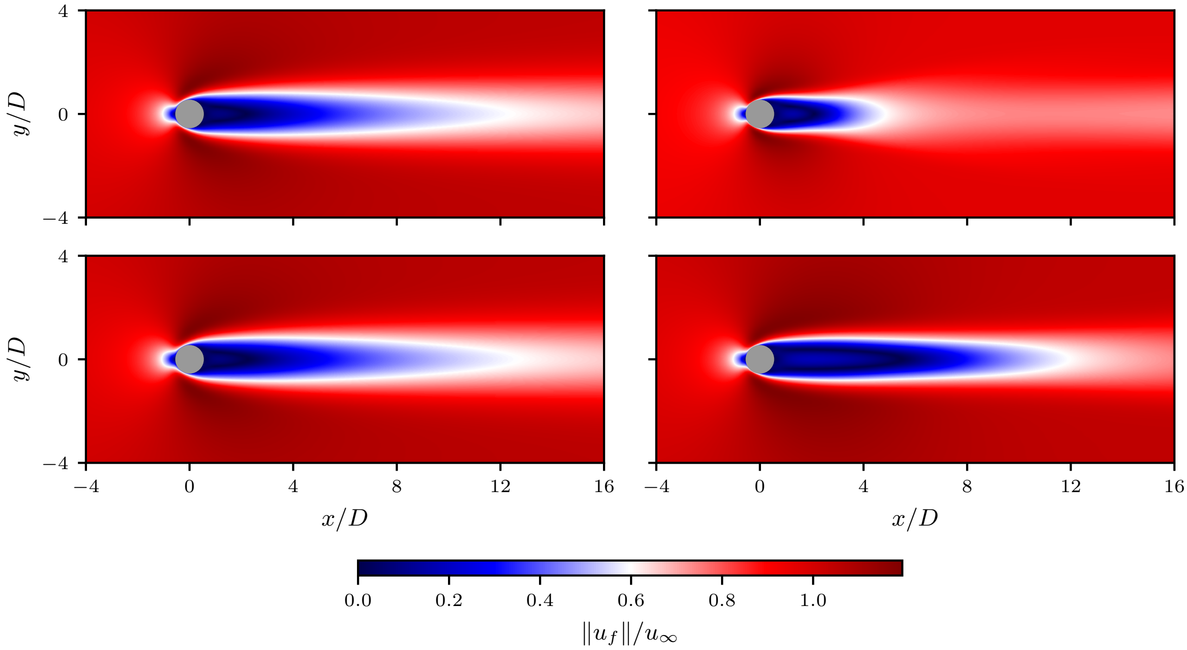

Figure 19: Time averaged fluid velocity magnitude at $\Theta_\infty = 10\%$; Top: Hydrogel; Bottom: Iron; Left: $\mathrm{Re}_{\mathrm{eff}} = 30$; Right: $\mathrm{Re}_{\mathrm{eff}} = 80$.

impact.

The relative velocity between particle and fluid (Fig. 21) is large at the stagnation point in front of the cylinder, where particles are moving very slowly due to frictional contact with the cylinder. The spatial extension of this low particle velocity region is increasing upstream when particle inertia is increased due to the progressive formation of the particle bow shock. At the edge of the recirculation zone, where we observe a non-uniform distribution of particles in the averaged flow fields, there is also a high relative velocity. Other regions with high relative velocity are the centers of the recirulation zone but interpretation can be flawed because these regions are almost free of particles .

6. Conclusion

This study utilizes efficient capabilities of the LBM to simulate particle-laden flows. Particle resolved simulations allow to investigate the unsteady response of particulate flows around a circular cylinder. To validate the computational model several configurations have been tested, such as single phase flow past a cylinder, granular drag coefficients and particle response to unsteady and shear forces. Our LBM-DEM delivers high accuracy since it is based on geometrically resolved moving bodies, while remaining sufficiently efficient to perform large simulations with hundreds of thousands of particles in decent computation time on a supercomputer. We decided to not account for gravity in order to disentangle the effects of mean slip velocity due to gravity from the inertia of particles.

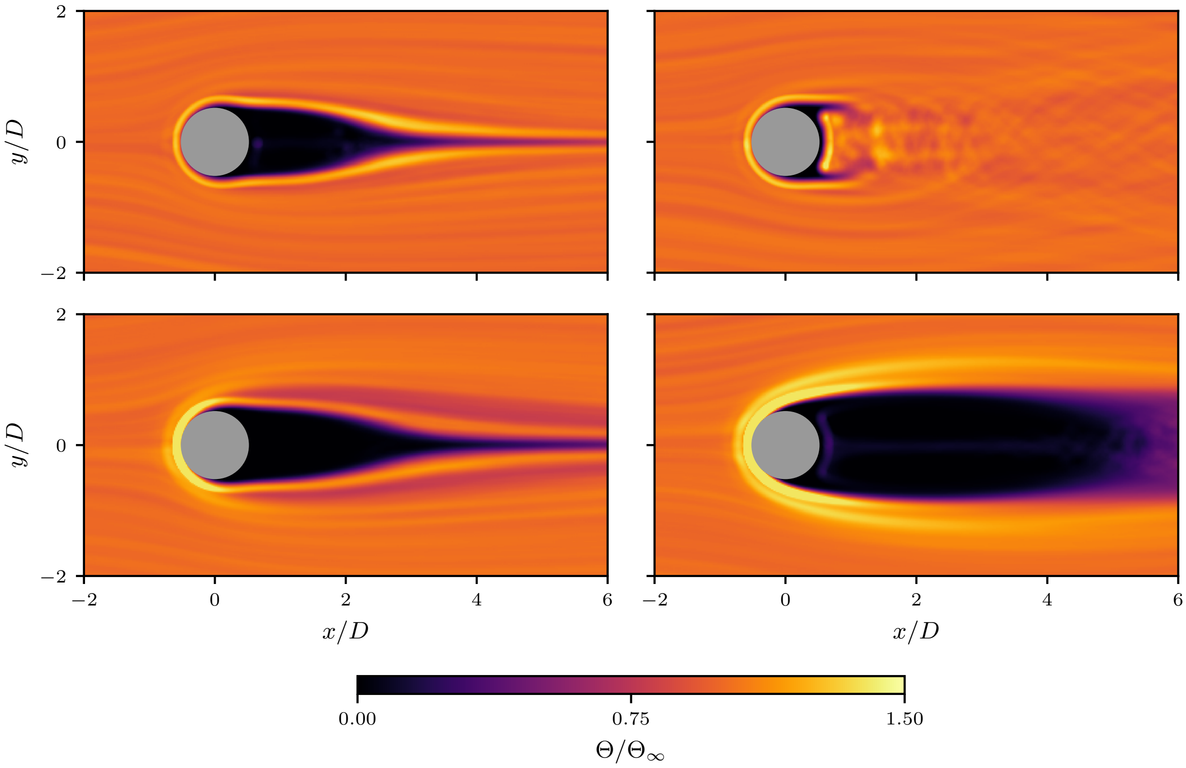

Figure 20: Time averaged spatial distribution of particle volume concentration at $\Theta_\infty = 10\%$. Top: Hydrogel; Bottom: Iron; Left: $\mathrm{Re}_{\mathrm{eff}} = 30$; Right: $\mathrm{Re}_{\mathrm{eff}} = 80$.

The predicted global flow parameters using an effective viscosity are well recovered for iso-dense and slightly inertial particles (typically glass beads in water) at a cylinder sphere diameter ratio equal to 5. Decreasing the particle size relative to the cylinder did not significantly change the drag coefficient and recirculation length predictions, except for points close to the onset of unsteady vortex shedding. We observe that steady wake is depleted of iso-dense particle as previously observed in microfluidic experiments while higher Reynolds flows are unsteady and von-Karman vortices are populated with particles because their Stokes number is low. Increasing particle inertia shows that the simple modeling of dispersed two-phase flows with mixture physical properties is not adequate to predict the drag force experienced by the cylinder.

Suspensions with relative density higher than 2.5 are more complex to describe due to the interplay between hydrodynamic and granular effects. In the steady regime, suspension flows exert a drag force similar to an equivalent fluid, but in the unsteady regime the evolution of the drag coefficient neither follows the prediction based on an equivalent fluid, nor as a granular flow. Inertia of particles forces them to cross the flow streamlines, leading to a stabilization of the wake zone depleted of particles and delaying the development of vortices. This yields global flow parameters to evolve in an intermediate regime between unsteady and steady response. We have observed that the spatial distribution of particles is depending

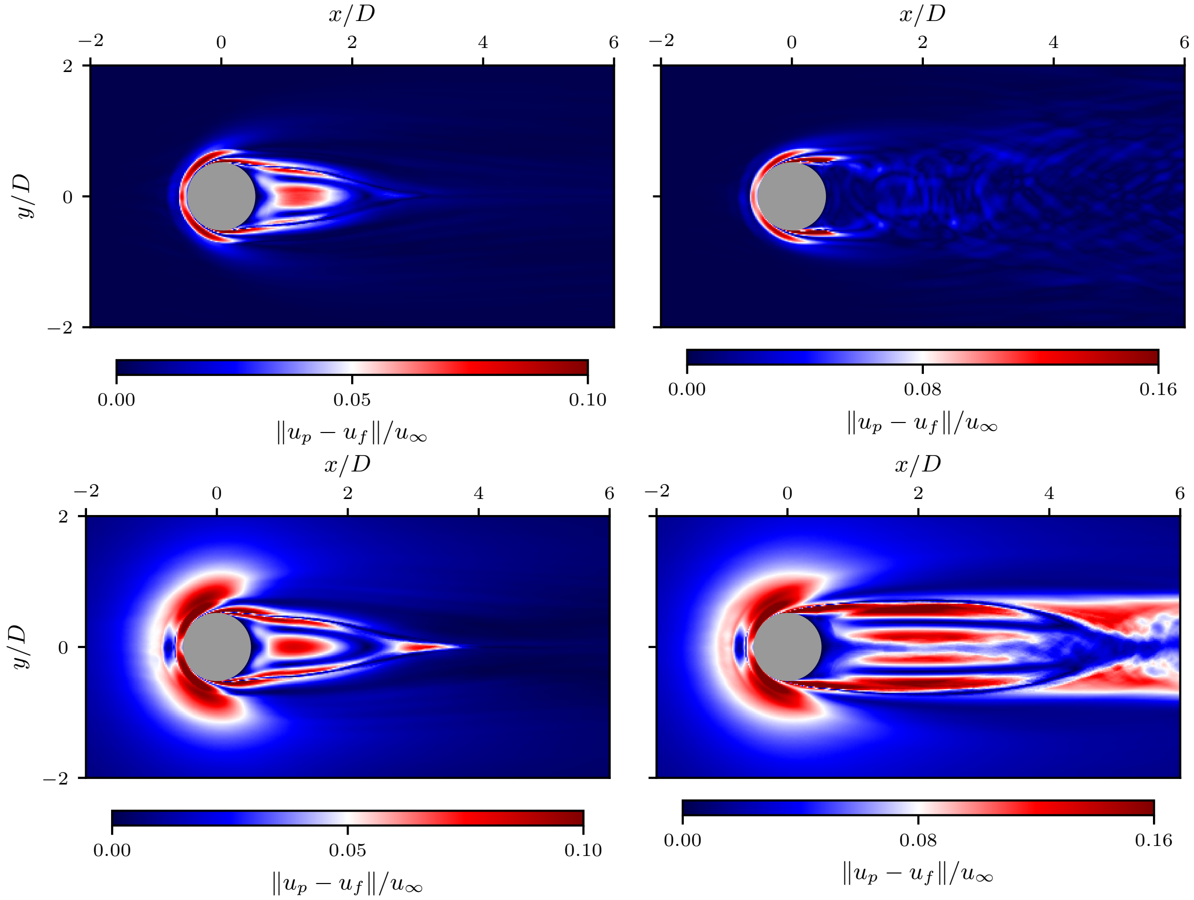

Figure 21: Time averaged relative velocity between particles and fluid at $\Theta_\infty = 10\%$. It is computed from the time averaged spatial distribution of the fluid velocity subtracted from the time averaged spatial distribution of the solid phase velocity. Top: Hydrogel; Bottom: Iron; Left: $\mathrm{Re}_{\mathrm{eff}} = 30$; Right: $\mathrm{Re}_{\mathrm{eff}} = 80$.

on the Stokes number characterizing the response time of particles. When Stokes number is equal to one or larger, the vortices are depleted of particles. Further simulations and experiments will be necessary to better predict flow parameters with a composite law including both hydrodynamic and granular features of suspensions at moderate relative densities.

At specific density ratios of $\mathcal{O}(100)$ or higher, the suspension largely resembles a granular flow, and a bow shock is present. The onset of von-Karman street is delayed. Drag coefficients are closer to the prediction for a dry granular material, even though the fluid contribution cannot be completely neglected.

Acknowledgments

The authors were granted access to the HPC resources of GENCI facilities at CINES, IDRIS and TGCC under the allocation #2020-A0082B11478. The authors would also like to thank the support and computational resources provided on Olympe supercomputer at CALMIP under the project P19040. Occitanie region is gratefully acknowledged for funding the PhD Thesis of D. Schuster under the project PALAFON.

References

[1] O. Stein, G. Olenik, A. Kronenburg, F. Marincola, B. Franchetti, A. Kempf, M. Ghiani, M. Vascellari, C. Hasse, Towards comprehensive coal combustion modelling for les, Flow Turbulence Combust 90 (2012) 859–884. doi:10.1007/s10494-012-9423-y.

[2] W. P. Adamczyk, G. Węcel, M. Klajny, P. Kozołub, A. Klimanek, R. A. Białecki, Modeling of particle transport and combustion phenomena in a large-scale circulating fluidized bed boiler using a hybrid Euler–Lagrange approach, Particuology 16 (2014) 29–40. doi:10.1016/j.partic.2013.10.007.
URL `https://www.sciencedirect.com/science/article/pii/S1674200113002265`

[3] S. Belošević, I. Tomanović, V. Beljanski, D. Tucaković, T. Živanović, Numerical prediction of processes for clean and efficient combustion of pulverized coal in power plants, Applied Thermal Engineering 74 (2015) 102–110. doi:10.1016/j.applthermaleng.2013.11.019.
URL `https://www.sciencedirect.com/science/article/pii/S1359431113008077`

[4] Y. Tang, Y. Lau, N. Deen, E. Peters, J. Kuipers, Direct numerical simulations and experiments of a pseudo-2D gas-fluidized bed, Chemical Engineering Science 143 (2016) 166–180. doi:https://doi.org/10.1016/j.ces.2015.12.026.
URL `https://www.sciencedirect.com/science/article/pii/S0009250915008039`

[5] A. Esteghamatian, A. Hammouti, M. Lance, A. Wachs, Particle resolved simulations of liquid/solid and gas/solid fluidized beds, Physics of Fluids 29 (3) (2017) 033302. arXiv:https://doi.org/10.1063/1.4979137, doi:10.1063/1.4979137.
URL `https://doi.org/10.1063/1.4979137`

[6] C. Rettinger, C. Godenschwager, S. Eibl, T. Preclik, T. Schruff, R. Frings, U. Rüde, Fully resolved simulations of dune formation in riverbeds, in: J. M. Kunkel, R. Yokota, P. Balaji, D. Keyes (Eds.), High Performance Computing, Springer International Publishing, Cham, 2017, pp. 3–21.

[7] F. Lachaussée, Y. Bertho, C. Morize, A. Sauret, P. Gondret, Competitive dynamics of two erosion patterns around a cylinder, Phys. Rev. Fluids 3 (2018) 012302. doi:10.1103/PhysRevFluids.3.012302.
URL `https://link.aps.org/doi/10.1103/PhysRevFluids.3.012302`

[8] K. Wieghardt, Experiments in granular flow, Annual Review of Fluid Mechanics 7 (1) (1975) 89–114. arXiv:https://doi.org/10.1146/annurev.fl.07.010175.000513, doi:10.1146/annurev.fl.07.010175.000513.
URL `https://doi.org/10.1146/annurev.fl.07.010175.000513`

[9] B. Percier, S. Manneville, J. N. McElwaine, S. W. Morris, N. Taberlet, Lift and drag forces on an inclined plow moving over a granular surface, Phys. Rev. E 84 (2011) 051302. doi:10.1103/PhysRevE.84.051302.
URL `https://link.aps.org/doi/10.1103/PhysRevE.84.051302`

[10] R. Soller, S. A. Koehler, Drag and lift on rotating vanes in granular beds, Phys. Rev. E 74 (2006) 021305. doi:10.1103/PhysRevE.74.021305.
URL `https://link.aps.org/doi/10.1103/PhysRevE.74.021305`

[11] T. A. Brzinski III, D. J. Durian, Characterization of the drag force in an air-moderated granular bed, Soft Matter 6 (2010) 3038–3043. doi:10.1039/B926180J.
URL `http://dx.doi.org/10.1039/B926180J`

[12] D. Quéré, Fluid coating on a fiber, Annual Review of Fluid Mechanics 31 (1) (1999) 347–384. arXiv:https://doi.org/10.1146/annurev.fluid.31.1.347, doi:10.1146/annurev.fluid.31.1.347.
URL `https://doi.org/10.1146/annurev.fluid.31.1.347`

[13] L. E. Scriven, Physics and applications of dip coating and spin coating, MRS Proceedings 121 (1988) 717.

[14] W. Shi, M. J. Anderson, J. B. Tulkoff, B. S. Kennedy, J. B. Boreyko, Fog harvesting with harps, ACS Applied Materials & Interfaces 10 (14) (2018) 11979–11986, pMID: 29587482. arXiv:https://doi.org/10.1021/acsami.7b17488, doi:10.1021/acsami.7b17488.
URL `https://doi.org/10.1021/acsami.7b17488`

[15] F. Lachaussée, Y. Bertho, C. Morize, A. Sauret, P. Gondret, Competitive dynamics of two erosion patterns around a cylinder, Phys. Rev. Fluids 3 (2018) 012302. doi:10.1103/PhysRevFluids.3.012302.
URL `https://link.aps.org/doi/10.1103/PhysRevFluids.3.012302`

[16] S. Athani, P. Rognon, Inertial drag in granular media, Phys. Rev. Fluids 4 (2019) 124302. doi:10.1103/PhysRevFluids.4.124302.
URL `https://link.aps.org/doi/10.1103/PhysRevFluids.4.124302`

[17] B. Andreotti, Y. Forterre, O. Pouliquen, Granular Media: Between Fluid and Solid, Cambridge University Press, 2013. doi:10.1017/CBO9781139541008.

[18] T. Krüger, D. Holmes, P. V. Coveney, Deformability-based red blood cell separation in deterministic lateral displacement devices—A simulation study, Biomicrofluidics 8 (5) (2014) 054114. doi:10.1063/1.4897913.
URL `https://aip.scitation.org/doi/abs/10.1063/1.4897913`

[19] R. Albert, M. A. Pfeifer, A.-L. Barabási, P. Schiffer, Slow drag in a granular medium, Phys. Rev. Lett. 82 (1999) 205–208. doi:10.1103/PhysRevLett.82.205.
URL `https://link.aps.org/doi/10.1103/PhysRevLett.82.205`

[20] U. Tüzün, R. Nedderman, Gravity flow of granular materials round obstacles—i: Investigation of the effects of inserts on flow patterns inside a silo, Chemical Engineering Science 40 (3) (1985) 325–336. doi:https://doi.org/10.1016/0009-2509(85)85095-8.
URL `https://www.sciencedirect.com/science/article/pii/0009250985850958`

[21] A. Tripathi, D. V. Khakhar, Numerical simulation of the sedimentation of a sphere in a sheared granular fluid: A granular stokes experiment, Phys. Rev. Lett. 107 (2011) 108001. doi:10.1103/PhysRevLett.107.108001.
URL `https://link.aps.org/doi/10.1103/PhysRevLett.107.108001`

[22] J. F. Boudet, H. Kellay, Drag coefficient for a circular obstacle in a quasi-two-dimensional dilute supersonic granular flow, Phys. Rev. Lett. 105 (2010) 104501. doi:10.1103/PhysRevLett.105.104501.
URL `https://link.aps.org/doi/10.1103/PhysRevLett.105.104501`

[23] C. R. Wassgren, J. A. Cordova, R. Zenit, A. Karion, Dilute granular flow around an immersed cylinder, Physics of Fluids 15 (11) (2003) 3318–3330. doi:10.1063/1.1608937.
URL `https://doi.org/10.1063/1.1608937`

[24] P. Jalali, Flow characteristics and stresses on cylindrical objects immersed in a flow of inelastic hard disks, Powder Technology 219 (2012) 217 – 227. doi:https://doi.org/10.1016/j.powtec.2011.12.047.
URL `http://www.sciencedirect.com/science/article/pii/S0032591011007303`

[25] S. Longo, A. Valiani, L. Lanza, Experiments on the two-dimensional flow of a grain–water mixture past a circular cylinder, European Journal of Mechanics - B/Fluids 36 (2012) 139–151. doi:https://doi.org/10.1016/j.euromechflu.2012.04.002.
URL `https://www.sciencedirect.com/science/article/pii/S0997754612000532`

[26] F. S. Seguin A., Lefebvre-Lepot A., P. P. Gondret, Clustering and flow around a sphere moving into a grain cloud, Eur. Phys. J. E 39 (63). doi:10.1140/epje/i2016-16063-0.
URL `https://doi.org/10.1140/epje/i2016-16063-0`

[27] A. Seguin, P. Gondret, Added-mass force in dry granular matter, Phys. Rev. E 105 (2022) 054903. doi:10.1103/PhysRevE.105.054903.
URL `https://link.aps.org/doi/10.1103/PhysRevE.105.054903`

[28] H. Homann, J. Bec, Concentrations of inertial particles in the turbulent wake of an immobile sphere, Physics of Fluids 27 (5) (2015) 053301. arXiv:https://doi.org/10.1063/1.4919723, doi:10.1063/1.4919723.
URL `https://doi.org/10.1063/1.4919723`

[29] Z. Shi, F. Jiang, H. Strandenes, L. Zhao, H. I. Andersson, Bow shock clustering in particle-laden wetted cylinder flow, International Journal of Multiphase Flow 130 (2020) 103332. doi:https://doi.org/10.1016/j.ijmultiphaseflow.2020.103332.
URL `http://www.sciencedirect.com/science/article/pii/S0301932220300562`

[30] K. Luo, J. Fan, W. Li, K. Cen, Transient, three-dimensional simulation of particle dispersion in flows around a circular cylinder Re=140–260, Fuel 88 (7) (2009) 1294–1301. doi:https://doi.org/10.1016/j.fuel.2008.12.026.
URL `https://www.sciencedirect.com/science/article/pii/S0016236108005292`

[31] H. Haddadi, S. Shojaei-Zadeh, K. Connington, J. F. Morris, Suspension flow past a cylinder: particle interactions with recirculating wakes, Journal of Fluid Mechanics 760 (2014) R2. doi:10.1017/jfm.2014.613.

[32] H. Haddadi, S. Shojaei-Zadeh, J. F. Morris, Lattice-Boltzmann simulation of inertial particle-laden flow around an obstacle, Phys. Rev. Fluids 1 (2016) 024201. doi:10.1103/PhysRevFluids.1.024201.
URL `https://link.aps.org/doi/10.1103/PhysRevFluids.1.024201`

[33] Y. H. Qian, D. D'Humières, P. Lallemand, Lattice BGK models for navier-stokes equation, Europhysics Letters (EPL) 17 (6) (1992) 479–484. doi:10.1209/0295-5075/17/6/001.
URL `https://doi.org/10.1209/0295-5075/17/6/001`

[34] X. He, L.-S. Luo, Lattice Boltzmann Model for the Incompressible Navier–Stokes Equation, Journal of Statistical Physics 88 (3) (1997) 927–944. doi:10.1023/B:JOSS.0000015179.12689.e4.
URL `https://doi.org/10.1023/B:JOSS.0000015179.12689.e4`

[35] P. L. Bhatnagar, E. P. Gross, M. Krook, A model for collision processes in gases. I. Small amplitude processes in charged and neutral one-component systems, Physical review 94 (3) (1954) 511.

[36] I. Ginzburg, F. Verhaeghe, D. d'Humieres, Two-relaxation-time lattice Boltzmann scheme: About parametrization, velocity, pressure and mixed boundary conditions, Communications in computational physics 3 (2) (2008) 427–478.

[37] I. Ginzburg, Study of simple hydrodynamic solutions with the two-relaxation-times lattice boltzmann scheme, Communications in Computational Physics.

[38] I. Ginzburg, D. d'Humières, A. Kuzmin, Optimal Stability of Advection-Diffusion Lattice Boltzmann Models with Two Relaxation Times for Positive/Negative Equilibrium, Journal of Statistical Physics 139 (6) (2010) 1090–1143. doi:10.1007/s10955-010-9969-9.
URL `https://doi.org/10.1007/s10955-010-9969-9`

[39] T. Krüger, H. Kusumaatmaja, A. Kuzmin, O. Shardt, G. Silva, E. M. Viggen, The lattice Boltzmann method: principles and practice, Springer Berlin Heidelberg, New York, NY, 2016.

[40] A. J. C. Ladd, Numerical simulations of particulate suspensions via a discretized Boltzmann equation. part 1. theoretical foundation, Journal of Fluid Mechanics 271 (1994) 285–309. doi:10.1017/S0022112094001771.

[41] C. K. Aidun, Y. Lu, E.-J. Ding, Direct analysis of particulate suspensions with inertia using the discrete Boltzmann equation, Journal of Fluid Mechanics 373 (1998) 287–311.

[42] B. Wen, C. Zhang, Y. Tu, C. Wang, H. Fang, Galilean invariant fluid–solid interfacial dynamics in lattice Boltzmann simulations, Journal of Computational Physics 266 (2014) 161–170. doi:10.1016/j.jcp.2014.02.018.
URL `http://linkinghub.elsevier.com/retrieve/pii/S0021999114001387`

[43] J. Götz, K. Iglberger, C. Feichtinger, S. Donath, U. Rüde, Coupling multibody dynamics and computational fluid dynamics on 8192 processor cores, Parallel Computing 36 (2) (2010) 142–151. doi:https://doi.org/10.1016/j.parco.2010.01.005.
URL `https://www.sciencedirect.com/science/article/pii/S0167819110000165`

[44] D. Bartuschat, U. Rüde, Parallel multiphysics simulations of charged particles in microfluidic flows, Journal of Computa-

tional Science 8 (2015) 1–19. doi:https://doi.org/10.1016/j.jocs.2015.02.006.
URL `https://www.sciencedirect.com/science/article/pii/S1877750315000162`

[45] S. Tao, J. Hu, Z. Guo, An investigation on momentum exchange methods and refilling algorithms for lattice Boltzmann simulation of particulate flows, Computers & Fluids 133 (2016) 1–14. doi:https://doi.org/10.1016/j.compfluid.2016.04.009.
URL `https://www.sciencedirect.com/science/article/pii/S0045793016301116`

[46] C. Peng, Y. Teng, B. Hwang, Z. Guo, L.-P. Wang, Implementation issues and benchmarking of lattice Boltzmann method for moving rigid particle simulations in a viscous flow, Computers & Mathematics with Applications 72 (2) (2016) 349–374. doi:https://doi.org/10.1016/j.camwa.2015.08.027.
URL `https://www.sciencedirect.com/science/article/pii/S089812211500406X`

[47] M. R. Maxey, J. J. Riley, Equation of motion for a small rigid sphere in a nonuniform flow, The Physics of Fluids 26 (4) (1983) 883–889. arXiv:https://aip.scitation.org/doi/pdf/10.1063/1.864230, doi:10.1063/1.864230.
URL `https://aip.scitation.org/doi/abs/10.1063/1.864230`

[48] G. Wang, M. Abbas, E. Climent, Modulation of large-scale structures by neutrally buoyant and inertial finite-size particles in turbulent couette flow, Phys. Rev. Fluids 2 (2017) 084302. doi:10.1103/PhysRevFluids.2.084302.
URL `https://link.aps.org/doi/10.1103/PhysRevFluids.2.084302`

[49] P. A. Cundall, O. D. L. Strack, A discrete numerical model for granular assemblies, Géotechnique 29 (1) (1979) 47–65. arXiv:https://doi.org/10.1680/geot.1979.29.1.47, doi:10.1680/geot.1979.29.1.47.
URL `https://doi.org/10.1680/geot.1979.29.1.47`

[50] S. F. Foerster, M. Y. Louge, H. Chang, K. Allia, Measurements of the collision properties of small spheres, Physics of Fluids 6 (3) (1994) 1108–1115. arXiv:https://doi.org/10.1063/1.868282, doi:10.1063/1.868282.
URL `https://doi.org/10.1063/1.868282`

[51] T. Kempe, J. Frohlich, Collision modelling for the interface-resolved simulation of spherical particles in viscous fluids, Journal of Fluid Mechanics 709 (2012) 445–489. doi:10.1017/jfm.2012.343.

[52] V. Becker, T. Schwager, T. Pöschel, Coefficient of tangential restitution for the linear dashpot model, Physical Review E 77 (1). doi:10.1103/PhysRevE.77.011304.
URL `https://link.aps.org/doi/10.1103/PhysRevE.77.011304`

[53] C. Crowe, J. Schwarzkopf, M. Sommerfeld, Y. Tsuji, Multiphase flows with droplets and particles, CRC Press, 2011.

[54] A. G. Kidanemariam, M. Uhlmann, Interface-resolved direct numerical simulation of the erosion of a sediment bed sheared by laminar channel flow, International Journal of Multiphase Flow 67 (2014) 174–188. doi:https://doi.org/10.1016/j.ijmultiphaseflow.2014.08.008.
URL `https://www.sciencedirect.com/science/article/pii/S0301932214001505`

[55] C. Rettinger, U. Rüde, A coupled lattice Boltzmann method and discrete element method for discrete particle simulations of particulate flows, Computers & Fluids 172 (2018) 706–719. doi:https://doi.org/10.1016/j.compfluid.2018.01.023.
URL `https://www.sciencedirect.com/science/article/pii/S004579301830029X`

[56] Q. Li, M. Abbas, J. F. Morris, E. Climent, J. Magnaudet, Near-wall dynamics of a neutrally buoyant spherical particle in an axisymmetric stagnation point flow, Journal of Fluid Mechanics 892 (2020) A32. doi:10.1017/jfm.2020.185.

[57] Q. Li, M. Abbas, J. F. Morris, Particle approach to a stagnation point at a wall: Viscous damping and collision dynamics, Phys. Rev. Fluids 5 (2020) 104301. doi:10.1103/PhysRevFluids.5.104301.
URL `https://link.aps.org/doi/10.1103/PhysRevFluids.5.104301`

[58] J. C. Brändle de Motta, W.-P. Breugem, B. Gazanion, J.-L. Estivalezes, S. Vincent, E. Climent, Numerical modelling of finite-size particle collisions in a viscous fluid, Physics of Fluids 25 (8) (2013) 083302. doi:10.1063/1.4817382.
URL `https://doi.org/10.1063/1.4817382`

[59] M. Abbas, E. Climent, J.-F. Parmentier, O. Simonin, Flow of particles suspended in a sheared viscous fluid: Effects of

finite inertia and inelastic collisions, AIChE Journal 56 (10) (2010) 2523–2538. doi:https://doi.org/10.1002/aic.12192.
URL `https://aiche.onlinelibrary.wiley.com/doi/abs/10.1002/aic.12192`

[60] D. Legendre, R. Zenit, C. Daniel, P. Guiraud, A note on the modelling of the bouncing of spherical drops or solid spheres on a wall in viscous fluid, Chemical Engineering Science 61 (11) (2006) 3543 – 3549. doi:https://doi.org/10.1016/j.ces.2005.12.028.
URL `http://www.sciencedirect.com/science/article/pii/S0009250905009711`

[61] A. Ladd, R. Verberg, Lattice-Boltzmann simulations of particle-fluid suspensions, Journal of statistical physics 104 (5) (2001) 1191–1251. doi:10.1023/A:1010414013942.

[62] widely applicable Lattice Boltzmann from Erlangen, `http://walberla.net/`.

[63] C. Rettinger, U. Rüde, An efficient four-way coupled lattice Boltzmann – discrete element method for fully resolved simulations of particle-laden flows, Journal of Computational Physics 453 (2022) 110942. doi:https://doi.org/10.1016/j.jcp.2022.110942.
URL `https://www.sciencedirect.com/science/article/pii/S0021999122000043`

[64] M. Bauer, S. Eibl, C. Godenschwager, N. Kohl, M. Kuron, C. Rettinger, F. Schornbaum, C. Schwarzmeier, D. Thönnes, H. Köstler, U. Rüde, waLBerla: A block-structured high-performance framework for multiphysics simulations, Computers & Mathematics with Applications 81 (2021) 478 – 501. doi:https://doi.org/10.1016/j.camwa.2020.01.007.
URL `http://www.sciencedirect.com/science/article/pii/S0898122120300146`

[65] C. Feichtinger, S. Donath, H. Köstler, J. Götz, U. Rüde, WaLBerla: HPC software design for computational engineering simulations, Journal of Computational Science 2 (2) (2011) 105–112. doi:https://doi.org/10.1016/j.jocs.2011.01.004.

[66] C. Godenschwager, F. Schornbaum, M. Bauer, H. Köstler, U. Rüde, A framework for hybrid parallel flow simulations with a trillion cells in complex geometries, in: Proceedings of the International Conference on High Performance Computing, Networking, Storage and Analysis, SC '13, Association for Computing Machinery, New York, NY, USA, 2013, pp. 1–12. doi:10.1145/2503210.2503273.
URL `https://doi.org/10.1145/2503210.2503273`

[67] Jean Zay supercomputer, `http://www.idris.fr/eng/jean-zay/`.

[68] OCCIGEN supercomputer, `https://www.cines.fr/en/supercomputing-2/hardwares/the-supercomputer-occigen/`.

[69] A. Einstein, Eine neue Bestimmung der Moleküldimensionen, Annalen der Physik 324 (2) (1906) 289–306. arXiv:https://onlinelibrary.wiley.com/doi/pdf/10.1002/andp.19063240204, doi:https://doi.org/10.1002/andp.19063240204.
URL `https://onlinelibrary.wiley.com/doi/abs/10.1002/andp.19063240204`

[70] G. K. Batchelor, J. T. Green, The determination of the bulk stress in a suspension of spherical particles to order c^2, Journal of Fluid Mechanics 56 (3) (1972) 401–427. doi:10.1017/S0022112072002435.

[71] I. M. Krieger, T. J. Dougherty, A mechanism for non-newtonian flow in suspensions of rigid spheres, Transactions of the Society of Rheology 3 (1) (1959) 137–152. arXiv:https://doi.org/10.1122/1.548848, doi:10.1122/1.548848.
URL `https://doi.org/10.1122/1.548848`

[72] C.-H. Hsueh, P. F. Becher, Effective viscosity of suspensions of spheres, Journal of the American Ceramic Society 88 (4) (2005) 1046–1049. arXiv:https://ceramics.onlinelibrary.wiley.com/doi/pdf/10.1111/j.1551-2916.2005.00204.x, doi:https://doi.org/10.1111/j.1551-2916.2005.00204.x.
URL `https://ceramics.onlinelibrary.wiley.com/doi/abs/10.1111/j.1551-2916.2005.00204.x`

[73] H. Eilers, Die Viskosität von Emulsionen hochviskoser Stoffe als Funktion der Konzentration, Kolloid-Zeitschrift 97 (3) (1941) 313–321. doi:10.1007/BF01503023.
URL `https://doi.org/10.1007/BF01503023`

[74] T. Dbouk, A suspension balance direct-forcing immersed boundary model for wet granular flows over obstacles, Journal

of Non-Newtonian Fluid Mechanics 230 (2016) 68–79. doi:https://doi.org/10.1016/j.jnnfm.2016.01.003.
URL `https://www.sciencedirect.com/science/article/pii/S0377025716000069`